Materials Advances

ROYAL SOCIETY OF CHEMISTRY

PAPER

View Article Online
View Journal | View Issue

Cite this: *Mater. Adv.*, 2025, **6**, 6076

Synthesis optimization, adsorption properties and spectroscopic investigation of an NH_2-tagged Cu-based MOF with open metal sites†

Lotfi Boudjema,[ah] Anil Kumar Dahiya,[b] Ivan da Silva,[c] Diego Gianolio,[d] Izuchika Nduka,[b] Manfred Erwin Schuster,[e] Gea Theodora van de Kerkhof,[de] Paulina Kalinowska,[b] Emilio Borrego-Marin,[f] Jorge A. R. Navarro,[f] Valentina Colombo,[i] June McCorquodale,[gh] David C. Grinter,[d] Pilar Ferrer,[d] Georg Held,[d] C. Richard A. Catlow[agh] and Rosa Arrigo*[bd]

We report the rapid microwave-assisted solvothermal synthesis of a Cu-MOF (metal–organic framework) with open metal sites, focusing on understanding its CO_2 capture properties in relation to phase purity and stability. A combined experimental and theoretical approach is used to identify the MOF's structural features involved in the adsorption process. Specifically, Cu(I) defects are found to play an important role in the CO_2 adsorption process, with the Cu-1 sample, synthesized using an optimized ligand/Cu precursor ratio for the highest phase purity, exhibiting more abundant Cu(I) defects as well as the highest adsorption capacity. Grand canonical Monte Carlo simulations show that the Cu(I) sites exhibit a greater affinity for CO_2 adsorption compared to the Cu(II) sites. *In situ* soft and hard X-ray absorption fine structure spectroscopic techniques confirm the conversion of Cu(I) to Cu(II) upon CO_2 chemisorption, with this conversion being more pronounced in the core of the particles. The simulations are used to estimate the fraction of Cu(I) defects and Cu(II) sites present within the Cu-1 and to validate the experimental isotherm. Overall, this study provides insights into the CO_2 capture properties of this type of Cu-MOF and highlights the importance of phase purity and the role of defects in achieving high adsorption performance.

Received 23rd June 2025,
Accepted 25th June 2025

DOI: 10.1039/d5ma00666j

rsc.li/materials-advances

1. Introduction

The rising levels of greenhouse gases[1,2] provides a powerful incentive for the rapid development and implementation of effective low C technologies.[3] Current strategies for the containment of the emissions include CO_2 capture from combustion units by irreversible mineralization into solid carbonates or by reversible adsorption using basic liquid media (*e.g.* ammonium salts and ionic liquids) or highly porous solid materials (zeolites, carbon, and metal–organic frameworks (MOFs)).[4,5] The structural characteristics of MOFs hold promise for their use in selective gas capture and separation,[6] due to their flexible synthetic design in which ligands and metal sites are assembled *via* coordinative bonds, enabling the creation of tailored microstructures and functionalities together with the ability to withstand thermal and chemical changes.[7–9] The design of a selective MOF towards a specific gas requires the optimization of the adsorption energy of the gaseous molecules at the host sites. A high adsorption energy enhances the affinity of the material toward a specific gas, but if the interactions are too strong, the energy input required for desorption is too high, thus making the adsorption process irreversible or economically unviable. Exposed, fully-desolvated open metal sites (OMS) in a MOF play a major role in the selective capture, with Lewis acid metal sites highly efficient towards the capture of Lewis basic molecules and *vice versa*.[10]

[a] *Department of Chemistry, University College London, 20 Gordon Street, London, WC1H 0AJ, UK*
[b] *School of Science, Engineering and Environment, University of Salford, Manchester, M5 4WT, UK. E-mail: r.arrigo@salford.ac.uk*
[c] *ISIS Neutron and Muon Source, STFC Rutherford Appleton Laboratory, Didcot, Oxfordshire, OX11 0QX, UK*
[d] *Diamond Light Source Ltd., Harwell Science & Innovation Campus, Didcot, Oxfordshire, OX11 0DE, UK*
[e] *Johnson Matthey Technology Centre, Reading, RG4 9NH, UK*
[f] *Departamento de Química Inorgánica, Universidad de Granada, Av. Fuentenueva S/N, 18071 Granada, Spain*
[g] *Cardiff Catalysis Institute, School of Chemistry, Cardiff University, Main Building, Park Place, Cardiff, CF10 3AT, Wales, UK*
[h] *UK Catalysis Hub, Research Complex at Harwell, Rutherford Appleton Laboratory, R92, Harwell, Oxfordshire OX11 0FA, UK*
[i] *Università degli Studi di Milano, Dipartimento di Chimica, Via Golgi, 19, 20133 Milano, Italy*

† Electronic supplementary information (ESI) available. See DOI: https://doi.org/10.1039/d5ma00666j

In the field of CO_2 adsorption, an archetypal example is HKUST-1 (also denoted as $Cu_3(BTC)_2$, BTC = benzene-1,3,5-tricarboxylate).[11] In HKUST-1, OMS can be easily generated by removing the apical solvent molecules with gentle heating under low pressure, resulting in the activated structure with exposed Cu^{2+}. It is proposed that CO_2 can interact with the Cu^{2+} OMS in HKUST-1 after activation and removal of solvent molecules.[12] Moreover, recent evidence also suggests the involvement of defective Cu^{+} sites in the reversible adsorption of CO_2.[13]

Amination is another strategy to introduce NH_2 functionalities in a solid adsorbent, which are selective for CO_2 capture.[14] By using 5-aminoisophthalic acid as the ligand under solvothermal conditions of a mixture of water, ethanol and dimethyl formamide (DMF), Zhao *et al.* synthesised a Cu-based MOF, namely JUC-141, which was found to have high CO_2/N_2 selectivity values as well as a high adsorption enthalpy when compared to other MOFs.[15] This MOF is constructed using 5-aminoisophthalic acid (H_2AIPA) coordinated to Cu^{2+} cations *via* the carboxylic groups to form the classic paddle wheel secondary building units (SBU) and with the amino groups linked to the dipole of the paddle wheel to form a 3D porous framework.[15] The higher adsorption enthalpy is attributed to the strong interactions of CO_2 with the amino groups due to confinement effects within the channels.[15]

A similar Cu(II) MOF based on the 5-aminoisophtalic acid ligand (Cu(AIPA)) was synthesised by Xu *et al.*[16] *via* solvothermal synthesis using only DMF as the reaction solvent. This structure contains Cu paddle wheel units, similar to HKUST-1 and JUC-141, but now the amino groups belonging to the organic linkers are free and protrude into the pores of the system (Fig. 1), leading to a monoclinic structure. After removal of the DMF molecule coordinated to the Cu-paddle wheels, this synthesis afforded a MOF structure that is thermally stable above 500 K for over 36 h, with an interesting adsorption ability towards formaldehyde.[16]

In this work, we focus on the monoclinic Cu(AIPA) as a CO_2 adsorbent because the bimodal chemisorption sites present allow, in principle, selective gas sorption. The CO_2 adsorption capacity of this MOF was reported to be very similar to the value for JUC-141 (70 $cm^3\ g^{-1}$ and 79.95 $cm^3\ g^{-1}$ for Cu(AIPA)[16] and JUC-141,[15] respectively) but the surface area of the latter is approximately one order of magnitude higher, whereas the pore size is larger (14 Å in diameter for JUC-141 and 9.9 Å × 9.2 Å for Cu(AIPA)), which would be consistent with the hypothesis that the metal dimers play a primary role in the adsorption properties of this MOF towards CO_2.

The phase composition obtained is crucial for the adsorption properties of MOFs; however the impact of impurities on these properties has not been thoroughly investigated. Previous studies[15,16] demonstrate that the synthesis conditions have a profound influence on the product. For instance, variations in these conditions can lead to the formation of JUC-141, where the amino groups of the 5-aminoisophtalic acid ligands are involved in coordination, or GIF-KUC, where these groups remain uncoordinated. Ahnfeldt *et al.*[17] reported a systematic analysis for an Al-MOF, examining how factors such as the molar ratios of the metal salt to ligand, the choice of solvents, and the type of aluminum salts affect the resulting structure.

Their study revealed a strong sensitivity of the synthesis process to reaction conditions, leading to the formation of multiple known and unidentified phases across different compositions. This inherent complexity in phase behavior is likely to become even more pronounced during scale-up, potentially compromising the consistency of gas separation performance on a per-gram basis.

In this work, we report the optimization of a microwave-assisted solvothermal synthesis route for Cu(AIPA) metal–organic frameworks (MOFs), supported by a comprehensive structural analysis using both soft and hard X-ray absorption spectroscopy techniques, alongside powder X-ray diffraction. This approach enables the rapid and reproducible synthesis of phase-pure Cu(AIPA) MOFs under relatively mild conditions, while also leading to the formation of a wide variety of defect sites within the framework. Furthermore, we investigate the nature of the CO_2–MOF interaction through *in situ* X-ray absorption spectroscopy techniques, providing direct insight into the local coordination environment of the active sites. Complementary molecular modeling is employed to elucidate the underlying mechanisms of CO_2 capture at the atomic level, offering a detailed understanding of adsorption phenomena that are otherwise inaccessible through experimental methods alone.

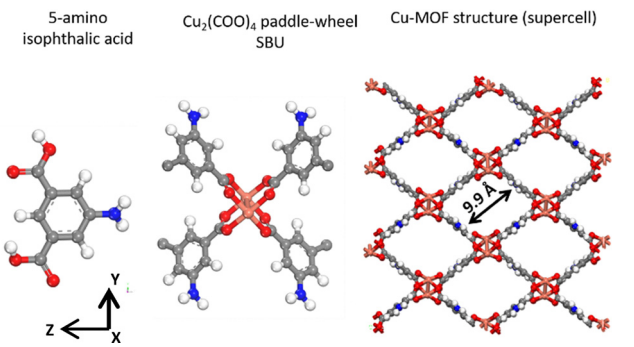

Fig. 1 Visualization of the monoclinic Cu(AIPA) structure represented as a 4 × 3 × 2 supercell (expanded along the *x*, *y*, and *z* crystallographic axes) and viewed along the *x*-direction. The atomic color scheme is as follows: copper (Cu) – orange; carbon (C) – grey; oxygen (O) – red; nitrogen (N) – blue; hydrogen (H) – white.

2. Experimental

2.1. Preparation of Cu metal–organic frameworks (GIF-KUC)

$Cu(NO_3)_2{\cdot}9H_2O$ (Sigma Aldrich 98%) and 5-amino isophthalic acid (5-AIPA) (Sigma Aldrich 94%) in different ratios were dissolved in 10 mL of DMF (Sigma Aldrich 99.8%) and stirred for 10 minutes. The solution was introduced in a 35 mL microwave reaction vessel (CEM) equipped with a Teflon lid. The closed reaction vessel was inserted in the microwave synthesizer (Discover SP, CEM) heated at 373 K with ramp as indicated in Table 1 and maintained at this temperature for

Table 1 Sample notations and synthesis conditions

	Synthesis conditions							
Sample notation	Cu : AIFA molar ratio	$Cu(NO_3)_2{\cdot}3H_2O$ (mg)	5-AIPA (mg)	DMF (mL)	T (K)	Reaction time (min)	Heating time (min)	Yield[a] (mg)
Cu-1	1.6	400	250	10	373	30	10	87
Cu-2	2.2	550	250	10	373	30	10	134
Cu-3	2.8	700	250	10	373	30	10	170
Cu-B1	1.6	400	250	10	373	30	10	n.d.
Cu-B2	1.6	400	250	10	373	30	2	84.8
Cu-B3	1.6	400	250	10	373	30	5	n.d.
Cu-B4	1.6	400	250	10	373	30	20	91
Cu-B5	1.6	400	250	10	373	30	1	n.d.
Cu-B6	1.6	400	250	10	373	30	10	81

[a] Using $Cu_2(AIPA)_2(DMF)_2$ as the empirical formula of an ideal Cu(AIPA) MOF (molecular weight: 635.58 g mol^{-1}), and considering AIPA (250 mg) as the limiting reagent, the theoretical yield is calculated to be 0.439 g. The actual yield of the nearly pure Cu-1 phase corresponds to 19.8%. If other phases are present, the so-calculated percentage yield is overestimated.

30 minutes. The molar ratio between the Cu nitrate and the 5-amino isophthalic acid was varied as summarized in Table 1. Accordingly, Cu-1, Cu-2 and Cu-3 were synthesized using a molar ratio of 1.6 : 1, 2.2 : 1 and 2.8 : 1, in 10 mL of DMF each time. After the thermal treatment, the samples were filtered under vacuum, washed twice with DMF and dried in a vacuum oven at 373 K for 12 hours. The amount of product obtained in milligrams was determined after the drying step. The samples were stored in a desiccator at room temperature in screw cap vials for further analysis of the crystals.

The reproducibility of the synthesis was thoroughly evaluated, and consistent trends in phase purity were confirmed as a function of the Cu : AIPA molar ratio. Additionally, we investigated the influence of microwave heating time and specifically, the time to reach the target temperature. These parameters were found to significantly affect the phase composition and defect distribution, providing further insight into the tunability of the synthesis process. For Cu-1, Cu-2 and Cu-3, the reactor was ramped up to the targeted temperature in 10 minutes. B1, B2, B3, B4, B5 and B6 represent a replica of Cu-1 but the reaction temperature was reached in 10, 2, 5, 20, 1 and 10 minutes, respectively.

To further remove DMF, an additional step of washing was performed on a set of samples. Accordingly, the solids recovered by filtration after the hydrothermal synthesis were washed with 10 mL of methanol three times and then dried under vacuum at 343 K for 12 hours. These samples are referred to as $Cu\text{-}1_{meth}$, $Cu\text{-}2_{meth}$, and $Cu\text{-}3_{meth}$. A Cu-BTC, otherwise named HKUST-1, was prepared for comparison as follows: 3.38 g of $Cu(NO_3)_2{\cdot}3H_2O$ (Sigma Aldrich 98%) was dissolved in 75 mL of distilled water and stirred until a clear solution was obtained. 2.94 g of benzene-1,3,5-tricarboxylic acid (BTC) (95% purity, Sigma Aldrich) was dissolved in 75 mL of ethanol (Sigma Aldrich, 99.5%) and stirred until a clear solution was obtained. The two solutions were mixed, and the resulting mixture was thermally treated at 403 K for 30 minutes using the microwave synthesizer (Discover SPCEM), operating at 200 W in a hermetically sealed glass vial. The solid recovered by filtration was washed with 10 mL of distilled water (three times) and then dried under vacuum at 373 K for 12 hours.

2.2. Computational methods

2.2.1. Construction of models. The Cu-1 MOF framework was modeled based on the crystal structure previously reported by Xu *et al.*[16] This structure, which originally contained DMF molecules, was modified by removing these molecules to explore the full adsorption potential of the MOF. The structure belongs to the $P21/c$ space group, with a unit cell consisting of 32 C, 20 H, 4 N, 16 O, and 4 Cu atoms and lattice parameters of 7.76215 Å × 10.6561 Å × 14.9981 Å with $\alpha = 90.00^\circ$, $\beta = 90.6552^\circ$, and $\gamma = 90.00^\circ$. A supercell of size 4 × 3 × 2 was constructed to simulate the adsorption experiments. Soft X-ray XANES measurements of the synthesised Cu(AIPA) MOF revealed two key features: (i) the presence of under-coordinated Cu(I) sites and (ii) coordination of $-NH_2$ groups from the 5-aminoisophthalic acid ligands. Previous studies have suggested that Cu(I) defects arise when only three ligands coordinate to the Cu paddlewheel unit.[18] Building on this, our adsorption isotherm modeling supports the existence of three distinct coordination states: Tetra-Cu(II) sites coordinated to four ligands; Tri-Cu(I) sites coordinated to three ligands; and Di-Cu(I) sites coordinated to two ligands. Additionally, we propose that the $-NH_2$ groups may directly coordinate to the paddlewheel unit, contributing to the defect landscape. These coordination states—Tetra-Cu(II), Tri-Cu(I), Di-Cu(I), and coordinated $-NH_2$ sites—were explicitly incorporated into our models for adsorption isotherm simulations. To investigate CO_2 adsorption behavior, three structural models were constructed (Fig. S1, ESI†): (i) a defect-free monoclinic Cu(AIPA) structure with 100% Cu(II) sites, modified only by the removal of DMF molecules, (ii) structures with artificial Cu(I) defect sites, generated by systematically removing organic ligands, (iii) defective structures with varying concentrations of Cu(I) sites, homogeneously distributed within the supercell, to replicate the experimental CO_2 adsorption isotherms. Details of all structures investigated are given in the ESI.†

2.2.2. Force fields and grand canonical Monte Carlo (GCMC) simulations. To optimize the Cu-MOF structures, we employed a force field originally developed by Zhao *et al.*,[19] specifically designed to model framework flexibility. This force field includes intramolecular potentials and charges calculated *via* the extended charge equilibration (qEq) method[20] using the

GULP software (see Table S1, ESI†). A full optimization of both cell parameters and atomic coordinates was conducted using these parameters, and the results were validated against experimental crystallographic data. The optimized lattice parameters for Cu(AIPA) showed good agreement with experimental values: a = 7.7215 Å (−1.3%), b = 10.4303 Å (−2.1%), c = 14.7728 Å (−1.5%), α = 90.00°, β = 90.6462° (−0.0099%), and γ = 90.00° (Table S2, ESI†). Average bond lengths and angles were evaluated, showing strong agreement with experimental values (Table S3, ESI†). The robustness of this force field was further supported by Zhao *et al.*,[19] who demonstrated its effectiveness in predicting CO_2 adsorption isotherms in HKUST-1 when accounting for framework flexibility. Similar findings were reported for MOF-5.[21,22] However, it is generally acknowledged that flexibility can significantly affect gas diffusivity, especially in systems with strong adsorbate/MOF interactions.[23] Mellot-Draznieks *et al.*[23] demonstrated large-scale cooperative atomic displacements (exceeding 4 Å) in MIL-88 upon solvent adsorption. Sladekova *et al.*[24] further emphasized key modeling parameters for reliable isotherm predictions. In line with these insights, we modeled our Cu-MOF as a flexible framework, especially for defect-containing models,[25–27] achieving better agreement with the experimental adsorption measurements compared to a rigid model. GCMC simulations were carried out using the DL-Monte code[28] to investigate the adsorption of CO_2, N_2, and H_2O. Periodic boundary conditions were applied in all three dimensions. Lennard-Jones (LJ) interactions were truncated at a spherical cutoff of 12 Å, and electrostatics were computed using the Ewald summation method[29] with a precision of 1.0×10^{-6} kcal mol^{-1}. A total of four Monte Carlo (MC) moves were employed, including translation, rotation, insertion, and deletion, and move acceptance was governed by the Metropolis algorithm.[30] The production and equilibration steps were set to 1.0×10^6 and 3×10^6. To account for framework flexibility, the structure was allowed to relax after each MC move. For CO_2, a three-site linear model was used, with LJ parameters and partial charges assigned to each atomic site. N_2 was treated as a linear molecule with two LJ sites on the nitrogen atoms and a third at the center of mass, also with partial charges. Water was described using the TIP4P/2005 model.[31] Parameters for adsorbates (Tables S4 and S5, ESI†) were taken from the literature,[32] and MOF–adsorbate interactions were modeled using the Lorentz–Berthelot mixing rules,[33] with LJ parameters sourced from the DREIDING force field.[34] Simulations were conducted at 298 K and 1 bar for both binary (CO_2/N_2) and ternary ($CO_2/N_2/H_2O$) gas mixtures. The CO_2/N_2 ratio for the binary system was fixed at 15 : 85. In the ternary mixture, the partial pressures were set to 0.14508/0.82212/0.0328 bar for $CO_2/N_2/H_2O$, respectively, with the H_2O pressure corresponding to 80% of the TIP4P/2005 water vapor pressure.

The isosteric heat of adsorption (Q) was calculated using DL-Monte as follows:

$$Q = RT - \left(\frac{\partial\langle v\rangle}{\partial\langle q\rangle}\right)_T \quad (1)$$

where $\langle v\rangle$ is the potential average of the adsorbed phase, $\langle q\rangle$ is the average uptake at temperature T, and R is the universal gas constant.[35]

To evaluate gas separation performance, we calculated the selectivity S(i/j) of Cu-MOF for binary and ternary gas mixtures using:

$$S = \left(\frac{\frac{q_i}{q_j}}{\frac{p_i}{p_j}}\right) \quad (2)$$

where (q) is the uptake of gas species (i and j) in mmol g^{-1} and (p_i and p_j) are their corresponding partial pressures in bar.

2.3. Characterization techniques

2.3.1. Dynamic CO_2 breakthrough experiments. The measurements were conducted on a Varian-300 GC equipped with a gas mass spectrometer Hiden Analytical HPR-20 R&D. Helium, CO_2 and nitrogen were used throughout the measurements. The humidified CO_2 mixtures were obtained by passing the dry nitrogen through a water bath (relative humidity = 85%; mixture $N_2 : CO_2$, 85 : 15).

Before the dynamic CO_2 breakthrough measurement, approximately 400 mg of the sample powder was placed in a stainless steel tube (i.d. 5.0 mm, length 50 mm) and activated at two different temperatures (413 K and 493 K) with helium flow (20 mL min^{-1}) for 1 hour. Once the sample was activated, the designated gas mixture $N_2 : CO_2$, 85 : 15 (20 mL min^{-1}) with different relative humidities (0/85%) was monitored until equilibrium was reached. In addition, the sample column was conditioned at two different temperatures (273 K and 298 K) to study its influence on the CO_2 capture properties of the material. Finally, the gas flow was switched to the column reactor for the measurement that was considered to be completed when the detected CO_2 concentration reached the initial values.

2.3.2. Thermal analysis and adsorption properties. Thermogravimetric analysis (TGA) was employed to evaluate the stability and composition of the MOF samples. The analysis was carried out using a Mettler Toledo TGA-5500 analyzer. The measurements were preformed from 303 to 1073 K (heating ramp 5 K min^{-1}) under air (25 mL min^{-1}). The TGA results informed the pretreatment the MOFs was subjected to before the nitrogen sorption experiments, which were conducted at 77 K using a Quadsorb instrument. N_2 and He were utilized as adsorbates and for free space corrections, respectively. During the measurement, the sample was cooled to 77 K using a liquid nitrogen bath. The data analyses were carried out using the QuadraWin software. Screening of the pre-treatment conditions prior to the adsorption measurements enabled us to optimise the procedure for the removal of the solvent molecules (DMF). The data are summarised in Table S6 (ESI†). The samples degassed at 393 K overnight at 1 Pa showed very low specific surface area, indicating that solvent removal was unsuccessful. Consequently, we proceeded with an additional step consisting of washing the previously degassed samples with methanol

followed by overnight drying at 353 K, under static atmospheric conditions in air. The samples were then subjected to another degassing step at 393 K overnight at 1 Pa, before the adsorption measurements. With this pre-treatment, the surface area remained still low. Therefore the degassing temperature was increased to 413 K and the degassing treatment was carried out for 3 hours at 1 Pa. This temperature was finally chosen for the N_2 isotherm screening studies as it enabled higher surface area, thus a more effective removal of the solvent. Moreover, nitrogen sorption experiments were also performed on selected samples (Cu-1 and Cu-1_{meth}) after a degassing step at 473 K for 1 h. XRD analysis shows that the structural characteristics are largely maintained (Fig. S11b and c, ESI†) after the degassing step at 473 K for 1 h.

2.3.3. Single CO_2 adsorption isotherms. Single CO_2 adsorption experiments were carried out on Cu-1 at 273 K and 298 K using a Micromeritics 3Flex volumetric instrument located in the laboratories at the University of Granada. Prior to measurement, the powder sample (approximately 400 mg) was heated at two different temperatures (413 K and 493 K) for 1 h to study its influence on the CO_2 adsorption, and subsequently outgassed to 10^{-1} Pa in a Micromeritics SmartVacPrep Module.

The isosteric heat of adsorption (Q) is determined from the experimental CO_2 adsorption isotherms measured at different temperatures using the Clausius–Clapeyron equation. Initially, adsorption isotherms are experimentally measured at two temperatures, 273 K and 298 K, using a Micromeritics 3Flex volumetric instrument, where the amount of CO_2 adsorbed is recorded across a wide pressure range. Specific adsorption amounts are then selected for analysis, typically 0.10, 0.25, 0.50, 0.75, and 0.9 mmol. For each temperature, the pressure corresponding to the chosen adsorption amounts is identified, resulting in pairs of (P,T) values.

Subsequently, the Clausius–Clapeyron equation is applied by plotting the natural logarithm of pressure ($\ln P$) against the reciprocal temperature ($1/T$) for each selected adsorption amount. The resulting $\ln P$ *vs.* $1/T$ plot yields a straight line, where the slope is proportional to the isosteric heat of adsorption ($-Q/R$), with R being the universal gas constant. Finally, the slope of the linear plot for each adsorption amount is used to estimate Q, providing insights into the temperature dependence of the adsorption isotherms. The CO_2 sorption isotherm was also carried out for selected samples at 273 K on the Quadsorb Instruments analyzer located at the Research Complex at Harwell, with the pressure ranging from 0 to 100 kPa. Prior to the analysis, the samples (approximately 100 mg) were degassed for 2 hours at 473 K and 1 Pa. Helium was used for free space corrections and an isothermal bath was used to adjust the sample temperature during measurements.

2.3.4. Soft-XAS measurements. Soft XAS spectra at the Cu L edges were measured at the VERSOX B07 branch B beamline of the synchrotron facility DLS[36] in 3.5 mbar He in total electron yield (TEY) mode, using a current amplifier, and fluorescence electron yield (TFY) mode, using a photodiode. The O K-, N K- and C K-edge spectra were measured in an ultra-high vacuum (UHV). The freshly prepared samples were deposited on an indium foil and transferred directly from the atmospheric environment to the vacuum (10^{-7} mbar) in the analysis chamber. The beamline settings were: 600 L mm^{-1} grating of the monochromator and fix-focus constant, cff 2–2.25.

A linear background subtraction was carried out before intensity normalization of the spectra in the energy window above the absorption resonances (965–980 eV). To study the beam damage of the samples, Cu L-edges NEXAFS were measured sequentially on the same spot using the fast and slow-motion mode of the monochromator (Fig. S2, ESI†). We note a non-negligible effect of the beam with time, especially in the slow mode. However, the first measurements recorded in the fast scanning mode of the monochromator can be safely considered representative of the actual initial structure and therefore these are used herein to discuss the impact of synthesis conditions on the electronic structure characteristics of the samples.

Soft XAS measurements under a CO_2 atmosphere were performed at the ISISS beamline at Helmholtz-Zentrum Berlin (HZB) using both TEY and Auger electron yield (EY). EY XAS spectra were recorded with an analyzer setting of 50 eV pass energy (E_p) and electron kinetic energies (KE) of 385 eV, 385 eV, 385 eV, and 240 eV for Cu L-, O K-, N K- and C K-edges, respectively. The beam-line settings were exit slit (ES) 111 μm × 180 μm and cff 2.25. XAS spectra in total electron yield (TEY) were recorded using a Faraday cup positioned near the sample in the APXPS chamber.

2.3.5. XAFS measurements. X-ray absorption experiments (EXAFS and XANES) were conducted at the B18 Core EXAFS beamline of a diamond light source, using the Pt-coated collimating and focusing mirrors and a Si(111) double-crystal monochromator. A couple of Pt-coated harmonic rejection mirrors were inserted before the first ion chamber and used to filter out photons with higher energy. The size of the beam at the sample position was *ca.* 1 mm (h) × 1 mm (v). The samples were pelletized and measured in air. The data were collected in fluorescence mode by means of a 36-element solid state germanium detector (K_{max} = 14), and the ion chamber before the sample was used for measurement of the incoming photons (I_0 filled with a mixture of 30 mbar of Ar and 1080 mbar of He to optimize sensitivity at 20% efficiency). Data were normalized using the Athena software with a linear pre-edge and polynomial post-edge background subtracted from the raw data.

Furthermore, spatially resolved X-ray absorption near edge spectroscopy (XANES) and X-ray fluorescence (XRF) measurements were performed at the I14 hard X-ray nanoprobe beamline at the diamond light source.[37] For *operando* experiments, the sample was placed in a gas environment with heating element (DENS solutions),[38] which was positioned on a kinematic mount. N_2 was flown through the cell at a rate of 0.449 mL min^{-1} and CO_2 was flown through at a rate of 1 mL min^{-1}. Point XANES spectra at the I14 beamline were obtained *ex situ*, by placing the sample on a silicon nitride window at room temperature and exposing to air. XRF data were collected using a four-element silicon-drift detector in the backscatter geometry (RaySpec, UK). By scanning the X-ray energy and collecting

XRF maps at multiple energies through the Cu absorption edge XANES maps were extracted. A dwell time of 10 ms per pixel per energy step was used for both the XRF and XANES maps, and dwell time was varied between 10 ms and 100 ms per energy step for the point XANES scans. XRF imaging was performed at 9.5 keV for measurements corresponding to point XANES measurements, and at 9 keV for measurements corresponding to the XANES maps. The size of the beam at the sample position, and therefore the spatial resolution of the scans, was 50 nm in diameter. Principal component and cluster analysis of the XANES scans was performed using MANTiS software.[39]

2.3.6. SEM and XRPD. Scanning electron microscopy (SEM) analyses were performed on a Zeiss Ultra SEM operating at acceleration voltages of 1.6 and 20 keV. X-ray powder diffraction (XRPD) measurements were performed on a Rigaku Smartlab diffractometer, working with Cu $K\alpha_1$ radiation and Bragg–Brentano geometry. The obtained diffraction pattern for each sample was Rietveld refined using TOPAS 5 software.

3. Results and discussion

3.1. Structural characteristics of the synthesized MOFs

The structure and morphology of the synthesised samples were evaluated by means of powder X-ray diffraction (PXRD) and scanning electron microscopy (SEM). Fig. 2a and b shows the PXRD Rietveld refinement and SEM photograph relative to Cu-1, respectively. Accordingly, under the synthesis conditions of this sample, an almost pure monoclinic Cu(AIPA) structure (GIFKUC in CCDC, deposition number 628816) is obtained, as indicated by the good Rietveld refinement results. A very small amount of $Cu_2(OH)_3NO_3$ (ICSD 201478) impurity is also visible in the diffractogram (green patterns in the diffractogram with a refined amount of less than 1%wt). The SEM images show that the morphology of the particles is homogeneous consisting of rhomboid-shaped particles with each side approximately 20 microns long; these particles correspond to the Cu(AIPA) phase. Smaller particles deposited on the rhomboidal particles could be intuitively attributed to the $Cu_2(OH)_3NO_3$ phase. Energy dispersive X-ray elemental mapping on this sample shows N accumulation on these small particles consistent with this assumption (Fig. S3, ESI†). Replicas of the synthesis confirm that the most crystalline and pure monoclinic Cu(AIPA) phase is obtained under the conditions used for Cu-1 (Cu-B6 and Cu-B4 in Fig. S4, ESI†). Increasing the amount of the Cu precursor during the synthesis is detrimental in terms of phase purity as shown by the PXRD and SEM data for Cu-2 and Cu-3 in Fig. 2c, d and e, f, respectively. Particularly, we can see that the most intense diffraction peak from the $Cu_2(OH)_3NO_3$ phase (peak at 12.8° 2θ) increases in intensity with increasing amount of Cu precursor used for the synthesis. The abundance of the small nanoparticles deposited on the surface of the rhomboidal particles consistently increases. However, we note other impurities appearing in the diffraction patterns at small angles (8.33° and 9.14° for Cu-2 and 7.10°, 8.5°, 9.15° and 9.40° for Cu-3), which could not be assigned to any known phase. Interestingly, in the SEM images of Cu-2 and Cu-3, these peaks correlate to the appearance of lamellar particles with a needle-like morphology (see the inset in Fig. 2f). Cu-3 contains the highest number of unknown impurity peaks in the diffraction pattern, which indicates that this is the least pure sample. Whilst these phases are consistently found in these samples, the phase composition varies not only due to the molar ratio of the ligand and metal precursor used, but some changes are observed when using a different heating ramp, with the slowest heating ramp producing a material (Cu-B4 in Fig. S4c and d, ESI†) with the lowest amount of the precursor-derived $Cu_2(OH)_3NO_3$ impurity phase, suggesting a better utilization of the Cu precursor. The Cu K-edge XANES and EXAFS spectra of the samples are reported in Fig. 3a and b, respectively. Accordingly, a weak resonance due to the quadrupolar 1s → 3d electron transition and the pre-edge peak due to the dipole-allowed 1s → 4p electron transition for Cu(II) species are found around 8977 eV and 8985 eV, respectively. A more pronounced resonance at 8980–8985 eV is also found in Cu(I) oxides;[40] notably, this feature is more defined for the more crystalline Cu-1 sample. The Cu-2 sample is characterized by a XANES spectrum, which closely resembles the spectrum of the Cu-BTC sample synthesised using Cu nitrate and BTC as a ligand as described in the experimental part; this spectrum is also consistent with literature data for HKUST-1.[41] The FT EXAFS spectra in Fig. 3b are very similar for all the samples in the first coordination shell, but a noticeable difference is visible in the second coordination shell, more pronouncedly for the Cu-2, which consistently presents features similar to those of the Cu-BTC sample. A Cu nitrate nonahydrate reference spectrum is measured under the same conditions for comparison, showing a very different 2nd coordination shell. Fig. S5a (ESI†) compares the experimental spectra with the simulated spectra for Cu-MOF phases from the CCDC (GIFKUC and RAWYAS MOFs) as well as the impurity phase $Cu_2(OH)_3NO_3$. The structural models of these MOFs are also reported in Fig. S6 (ESI†). We suggest that the experimental spectra differ from the simulated spectra because of the presence of various phases as well as coordinated DMF molecules, which were fully removed in the simulations. One should consider that when more than one phase is present, interference effects can significantly affect intensities and make EXAFS interpretation difficult. We have also investigated the impact of the washing with methanol on the structures of the freshly prepared samples. The XAFS data for these samples, indicated as Cu-1_{meth}, Cu-2_{meth} and Cu-3_{meth}, are reported in Fig. S5b and c (ESI†). These results confirm that the Cu-1 is the most crystalline and robust sample, showing only a minimal change upon methanol washing and thermal desorption (only a reduction in the intensity at 2.2 Å – non-phase corrected – is observed in the FT-EXAFS spectrum, due to the small amount of impurities phase). In contrast, the Cu-2_{meth} undergoes more pronounced changes when compared to the starting samples. The comparison of the FT-EXAFS spectra for the three methanol washed samples is shown in Fig. 3c. Cu-1_{meth} and Cu-2_{meth} are very similar, which is consistent with the XANES data, whereas Cu-3_{meth} presents a lower

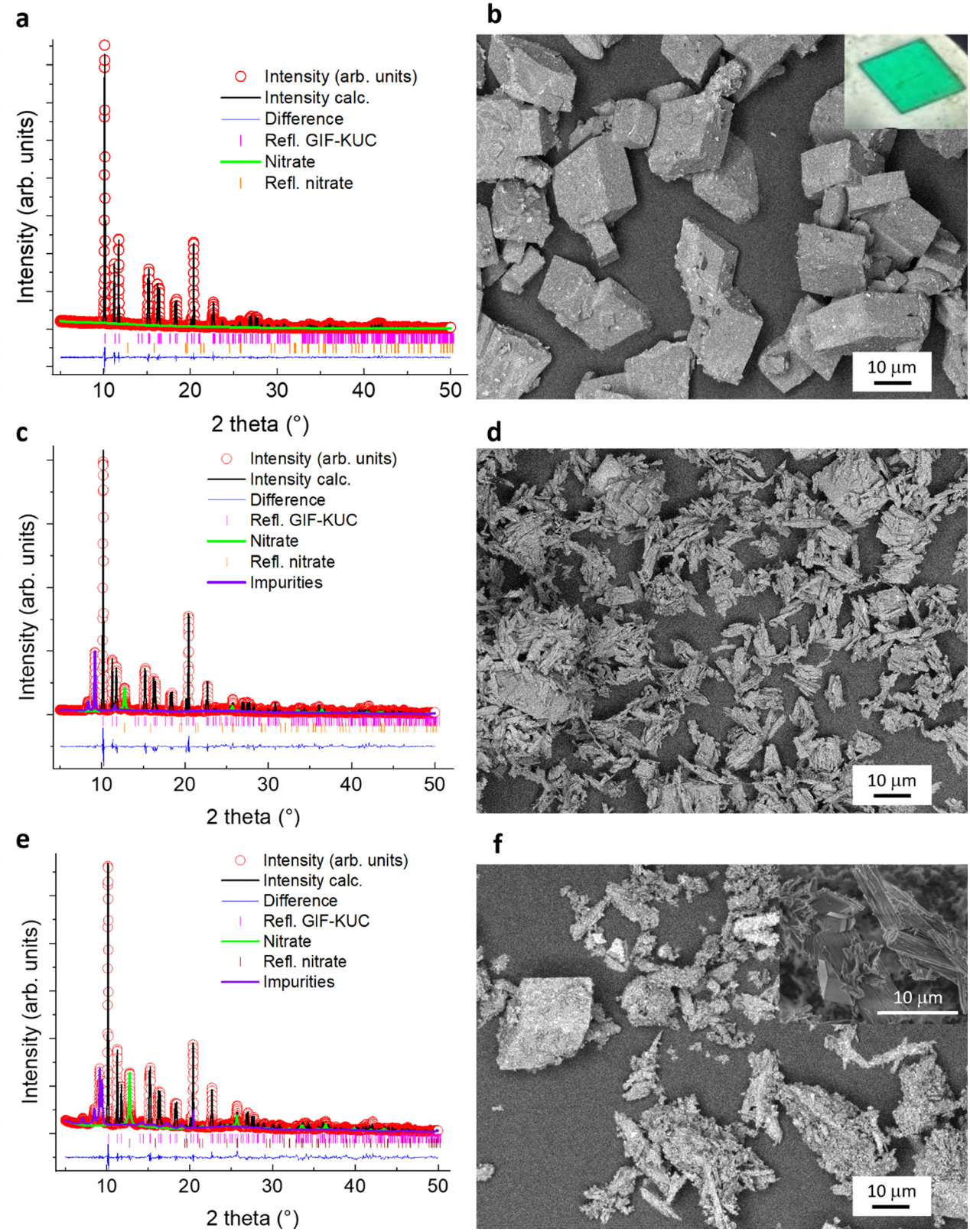

Fig. 2 Rietveld multiphase refined PXRD and SEM in the back scattering electron mode of Cu-1 (a and b); Cu-2 (c and d); and Cu-3 (e and f). Inset in (f) is a SEM in secondary electron mode.

coordination number in both the 1st and 2nd coordination shells. In general, lower intensity in the first coordination shell suggests a higher number of uncoordinated Cu defect sites or more structural disorder in terms of the bond length; in the 2nd

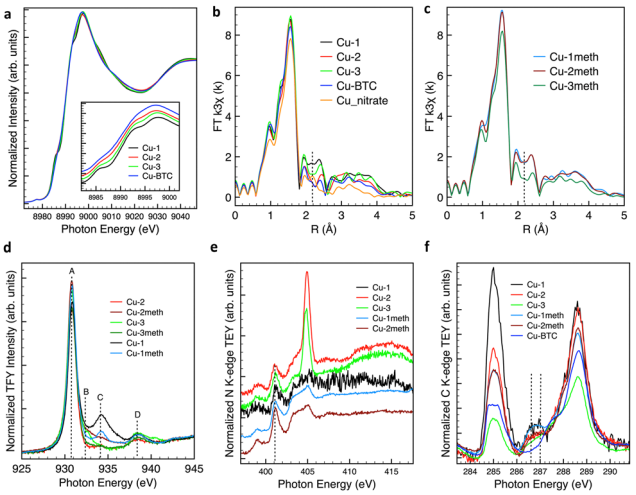

Fig. 3 XANES (a) and FT-EXAFS spectra (b) of Cu-1, Cu-2 and Cu-3. Spectra are compared with experimental data of Cu-BTC and Cu nitrate (Sigma Aldrich). (c) Comparison of the FT-EXAFS spectra of samples Cu-1, Cu-2 and Cu-3 experimental spectra after washing with methanol. (d) Cu L_3-edge XAFS spectrum of samples as indicated. (e) N K-edge XAFS and (f) C K-edge XAFS. The spectra in the inset in (a) are *y*-axis shifted for a better visualization.

coordination shell it can also imply a limited long-range order. Soft X-ray NEXAFS spectroscopy provides information on the electronic structure of elements with great surface sensitivity, when measured in TEY mode, while it is bulk-sensitive when measured in TFY mode. This implies that the TEY method will probe mainly the small particulate phases on the surface of the larger rhomboidal particles for samples containing a large fraction of these (*e.g.* Cu-2 and Cu-3). The Cu L_3-edge spectra in TFY of the synthesised samples are compared in Fig. 3d, whereas TEY spectra are reported in Fig. S5a (ESI†). Consistent with the literature,[18] the spectrum is characterized by four resonances, namely, A, B, C and D. Resonance A is unequivocally assigned to the Cu(II) ions of the Cu paddle-wheels SBUs, which are the predominant structural feature present in all the samples. However, a small peak C at approximately 934 eV indicates the existence of Cu(I) sites, more abundant on the most phase pure monoclinic Cu(AIPA) sample (Cu-1), which were associated with three-coordinated Cu(I) defects in the paddle wheels. Cu(I) sites are nevertheless omnipresent in the TFY (bulk) of all samples whereas found only in Cu-1, Cu-2 and Cu-1_{meth} in TEY mode (surface-sensitive). This indicates that for the Cu-2_{meth}, defective Cu(I) sites were generated in the bulk of the sample upon methanol washing treatment and subsequent thermal degassing treatment.

The resonance B is not found in the bulk of Cu-2 and is abundant in Cu-3; it is present in Cu-1 as well. A more intense B resonance is also formed in Cu-2_{meth} due to the methanol washing and heating treatment. The disappearance of the feature B upon thermal activation of HKUST-1 was associated with a thermally induced change of the Cu(II) coordination geometry, probably by the desorption of the solvent molecules.[18] The resonance D at 938.2 eV was found for H-adsorbed Cu(I) species,[42] but it is also due to the 2p → 4s electronic transition in the Cu^{2+} ions. Most of the changes observed upon washing involve the bulk of the samples with a reduction of the abundance of Cu(I) sites in Cu-1_{meth}, whereas these are formed in the case of the Cu-2_{meth}, consistent with the Cu K-edge XAFS data. Changes in the abundance of Cu(I) sites upon washing are intuitively linked to interaction of the solvent molecules (DMF or methanol) with these uncoordinated defective sites. In the case of the Cu-3_{meth}, no changes in the abundance of Cu(I) sites are seen, but the B resonance is now less visible, with a spectrum very similar to Cu-2. It is interesting to note that structural similarities between these two samples (Cu-2 and Cu-3_{meth}) were observed also in the EXAFS data (between 1.8 and 2.6 Å in Fig. S5c, ESI†) and related to secondary phases.

The analysis of the N K edge (Fig. 3e) reveals not only the π* resonances at 401.2 and 403.3 eV of DMF[43] but also a strong resonance at 405 eV attributed to NO_x species[44] more pronounced for the Cu-2 and Cu-3 samples. This species is related to the $Cu_2(OH)_3NO_3$ impurity phase more abundant on these samples. An additional π* resonance at 399 eV in all the samples is due to $-NH_2$ groups of the AIPA ligand. After washing with methanol and thermal treatment, the resonance at 405 eV in Cu-2_{meth} and Cu-3_{meth} is not as intense as in Cu-2 and Cu-3, respectively, indicating a successful removal of this NO_x-containing phase. The Cu-2_{meth} spectrum is very similar to those of Cu-1_{meth} and Cu-1, consistent with the other structural characterization data presented above. We note however that not all DMF was removed by the washing procedure. This indicates that DMF is actually strongly bound to some of the Cu sites and not fully removed during washing with methanol and vacuum desorption at 403 K. The O K-edge spectra of these samples (Fig. S5a, ESI†) are very similar to the spectrum reported for HKUST-1.[45] Two regions are identified: the sharp π* region around 532 eV due to 1s → O_{2p}–Cu_{3d} transitions and the broad σ* region around 540 eV due to 1s → O_{2p}–Cu_{4sp} transitions. The resonances in the intermediate region between 534 and 540 eV are due to C–O species. A similar conclusion can be drawn from the analysis of the O K-edge spectra of Cu-1 and Cu-2, with the latter one showing a much more intense π* resonance at 532 eV attributed to the Cu–O bond, possibly due to a bond N–C═O–Cu of coordinated—DMF[42] or due to the impurity $Cu_2(OH)_3NO_3$ phase. The O K-edge NEXAFS spectrum of Cu-2_{meth} resembles the spectrum of Cu-1, as expected when the abundance of the inorganic impurity phase is reduced.

In the C K-edge spectra in Fig. 3f, the expected contributions are from the ligand AIPA and the Cu-coordinated DMF for Cu-1, Cu-2 and Cu-3. For comparison we report here also the CK-edge of a Cu-BTC MOF, which does not contain DMF, as it was synthesised in an ethanol/water mixture. The main resonances found in Cu-BTC are assigned to transitions into the unoccupied π* orbitals of the phenyl system (~285 eV) and the carboxylate/carboxylic acid groups (~288 eV), similar to literature values for BPTCA.[46] The peak at 288 eV is also the most intense one in DMF and attributed to transition into the –N–C═O π* orbital. We can see that the relative intensity of these peaks is very similar for Cu-2, Cu-2_{meth} and Cu-1_{meth}, whereas Cu-1 presents a more intense π* orbital of the phenyl group

amongst the samples. Since the washing with methanol removes this component at 288 eV for Cu-1/Cu-1_{meth}, whereas the structure is maintained, we postulate that the surface of the Cu-1 is covered by carbonaceous species due to the residual, decarboxylated, uncoordinated ligand. This would be expected considering that the relative amount of AIPA used during this synthesis was the highest amongst the synthesis compositions investigated. Furthermore, we would like to understand if the removal of DMF can lead to structural distortion as indicated by the B resonance in the Cu L_3-edge spectra. An interesting aspect is evidenced with the analysis of Cu-2 and Cu-2_{meth}. When we compare Cu-2 with Cu-2_{meth} in Fig. 3f, the ratio between the two resonances (phenyl system (~285 eV) and the carboxylate/carboxylic acid groups (~288 eV)) remains almost unaltered after washing; therefore, we could assume that a negligible amount of DMF was removed from the surface/near surface region by this treatment and the signal of the C K-edge in this region is dominated by the ligand contribution. The interesting finding is related to the transitions around 288.3–288.7 eV, consistent with transitions of the type 1s → π* of C-NH_2 orbitals in the ligand, which are present with a relatively higher intensity in Cu-1 and Cu-1_{meth} than in Cu-2 and Cu-2_{meth}, whereas they are totally absent in Cu-BTC. We compare the Cu-2_{meth} and Cu-1_{meth} because these have a similar bulk structure (FT-EXAFS in Fig. 3c and XANES in Fig. S5c and d, ESI†) and similar content in terms of the nitrate impurity phase (NK edge spectrum in Fig. 3e). These two samples have the same intensity of ligand resonances (phenyl and carboxylates) but the 1s → π* C-NH_2 resonance is lower for Cu-2_{meth}. This can be attributed to either its decomposition during methanol washing/heating or a loss of direct or solvent-mediated coordination to Cu^{2+}. According to the Bly-holder model,[47] the resonance intensity in absorption spectroscopy is related to electronic effects induced by the ligation of the ligands L to the metal center M, with increase of the intensity of the resonance for a L to M π-donation, whereas a decrease in intensity occurs when also a π-back donation from M to L takes place.[47] It follows that such a coordination of the C–NH_2 moieties would be even more pronounced for the Cu-2, consistent with the fact that Cu-2 has a similar first and second coordination shell to the Cu-BTC (Fig. 3b). Such a site is however unstable during the thermal treatment of the washing process, which removes the coordination to NH_2 leaving Cu(I) sites in the main monoclinic Cu(AIPA) phase. Based on the similar spectrum of the Cu-2 with the Cu-BTC one might speculate that the NH_2 moiety of the AIPA ligands might interact with the Cu sites of the paddle wheels, generating a saturated Cu(II) coordination environment similar to HKUST-1 (Fig. S6c, ESI†). The morphological characteristics of this sample would suggest the presence of another phase, which however we were unable to assign (Fig. 2c and d). The thermal treatment following the methanol washing procedure is effective for the removal of this phase leading to a phase transformation that stabilizes the Cu(AIPA) (CCDC, deposition number 628816) phase, in which the AIPA-NH_2 group is not interacting anymore with Cu sites (Fig. S1c, ESI†), leading however to the formation of Cu(I) defective sites (resonance C in Fig. 3d) and other structural distortions (resonance B in Fig. 3d). This additional coordination could also explain the additional peaks in the diffractogram of Cu-2, but we have not pursued this further. Cu-3 exhibits greater structural complexity and heterogeneity. The lower intensity of the C K edge resonances for the Cu-3 is consistent with a surface dominated by the inorganic NO_x-containing phase as expected from the highest amount of Cu nitrate precursor used during the synthesis of this sample. Based on these results, we postulate that, during the several synthesis steps, the favored coordination of Cu(II) to carboxylate species of the ligands ultimately drives the phase transformations towards the target phase. However, when Cu(II) species are in excess –NH_2 groups remain coordinated hindering the crystallization of the target phase.

3.2. Textural properties

The Brunauer–Emmett–Teller (BET) surface area and pore volume as determined by N_2-adsorption isotherms for all the samples are summarized in Table 2. The N_2 isotherms are reported in Fig. S7 (ESI†), whereas the thermogravimetric analyses are reported in Fig. S8 (ESI†). The value of BET surface area and pore volume are significantly lower than the one reported for the same structure.[15] From the isotherm profile, it is possible to infer that the lower surface area could be due to the milder degassing pre-treatment conditions (413 K and 1 Pa for 1 h), which preceded the N_2 adsorption experiment in our investigation, being less effective at removing the molecules of the solvent within the micropores. However, the samples synthesised in this study also exhibit pore sizes significantly larger than the 0.99 nm value calculated from the crystallographic data.[16] This discrepancy suggests a substantial deviation from the ideal crystalline structure, likely resulting from the rapid microwave-assisted solvothermal synthesis, which promotes the formation of structural defects and disorder within the framework.

The monoclinic Cu(AIPA) structure was described as formed by 2D sheets generating a 3D framework through non-classical

Table 2 Specific BET surface area and pore volume[a]

Sample	Cu-1	Cu-1_{meth}	Cu-2	Cu-2_{meth}	Cu-3	Cu-3_{meth}
S_{BET}/m^2 g^{-1}	267	349	191	83	286	71
Pore volume (DFT method)/cm^3 g^{-1}	0.238	0.32	0.203	0.085	0.215	0.079
Pore size diameter (DFT method)/nm	5.88	4.15	4.88	5.68	4.89	2.77

[a] Samples were subjected to degassing at 413 K for 3 h at 1 Pa before N_2 physisorption.

hydrogen bond interactions between C–H groups in a benzene ring from one layer and a doubly bridging carboxyl oxygen atoms from the adjacent layer. Thus, parallel layers are coupled through these weak hydrogen bond interactions, forming a 3D supramolecular framework. We suggest that the local disorder of the H bond networks between layers is responsible for the larger pore size obtained and thus a lower surface area. The shape of the isotherm changes sharply with the degassing pre-treatment (Fig. S7b, ESI†) and provides more insights into the porous characteristics of these samples. At the lower degassing temperature (393 K, overnight) corresponding to very low surface areas as summarized in Table S6 (ESI†), the isotherm presents the type H3 hysteresis typical of slit-shaped meso- and macropores in materials with a plate-like layered structure, whereas the micropores are not accessible during our experiments. When the degassing is performed at higher temperature (413 K, 3 hours), the isotherm presents multistep-like behaviour in both the adsorption and desorption branches and a larger hysteresis loop, which is generally observed in highly flexible aggregates of plate-like particles[48] or when the macropores are filled with pore condensates. It was also reported for pore structures containing both open and partially blocked mesopores.[48] The abrupt changes observed in the desorption branch of the isotherms of these samples indicate a layer-to-layer structural instability during the adsorption experiments, consistent with higher interlayer flexibility due to a more disordered H-bonding network between the layers. The resulting surface area and in Table 2 is very similar for Cu-1 and Cu-3 and slightly lower for Cu-2. We should also note that only Cu-1 is an almost pure monoclinic Cu(AIPA) phase with larger primary particles free from deposits of secondary phases, whereas Cu-2 and Cu-3 present additional phases deposited on the primary particles, which will contribute to the adsorption behaviour.

Washing with methanol followed by thermal treatment was effective to a certain extent to remove carbonaceous impurities as well as accessible DMF molecules as shown with an increase of the surface area and pore volume for the Cu-1, Cu-1_{meth} system, confirming that this is the most structurally stable sample. In contrast, the BET surface area and pore volume are significantly reduced upon methanol treatment for Cu-2/Cu-2_{meth} and Cu-3/Cu-3_{meth} systems, indicating the poor stability of the other porous unknown phases contained in these samples and the more defective Cu(AIPA) phase. The thermogravimetric (TG) analysis of Cu-1 in Fig. S8a (ESI†) shows the DMF removed by methanol washing, amounting to 2% by weight. The TG analysis (Fig. S8b, ESI†) for Cu-2 indicates the presence of water in the pores as well as DMF, accounting for the 19% by weight. The washing step with methanol enables a more effective exchange of the DMF, leading to a very similar residual DMF content of this sample to Cu-1_{meth}, around 10%. However, this results in a loss of more than half the surface area, which means that these impurity phases, different from the monoclinic Cu(AIPA), are not suitable for gas adsorption studies. Interestingly, on Cu-3_{meth}, the amount of weakly chemisorbed adsorbates increases, indicating a further phase transformation generating adsorbed water. The TG analysis of these samples indicates that DMF desorption occurs in the range between 463 and 513 K, whereas the onset temperature at which the structure collapses is 533 K followed by two thermal processes with maximum rates at 547 K, 557 K and 563 K (Fig. S8, ESI†). Samples containing impurities such as Cu-2 and Cu-3 show a more complex thermal desorption profile, in which the first peak is less intense (Fig. S8, ESI†). This peak can be attributed to the decomposition of the carboxylate species of the ligands, which were used at higher concentrations in the synthesis, leading to the formation of the purest Cu(AIPA) phase.

3.3. CO_2 adsorption

3.3.1. Experimental data of the adsorption isotherm. CO_2 adsorption studies focused on the Cu-1 system, a nearly pure monoclinic Cu(AIPA) phase suitable for molecular modeling. Impurity phases reduce the capture properties of this MOF (Table 2 and Table S6, ESI†); therefore, Cu-1 was chosen for its superior physicochemical characteristics and more stable textural properties compared to Cu-2 and Cu-3.

The CO_2 adsorption isotherms of Cu-1 are plotted in Fig. 4a. From the conditions we explored in this work, it is clear that the uptake capacity of CO_2 for this sample depends on the activation pre-treatment as well as the temperature at which the adsorption is carried out. When the activation is carried out at 413 K and 0.1 Pa for 1 hour, the CO_2 uptake at saturation is $\sim$1.86 mmol g^{-1} and 0.93 mmol g^{-1} at 273 K and 298 K, respectively, both measured at 100 kPa. When the activation is carried out at 493 K, the CO_2 uptake at saturation is $\sim$1.46 mmol g^{-1} and 0.15 mmol g^{-1} at 273 K and 298 K, respectively, both measured at 100 kPa. The isosteric heat of adsorption presents a maximum value of 40 kJ mol^{-1}, which is accounted globally as a physisorption process, and decreases slowly with the amount of CO_2 adsorbed (Fig. S9, ESI†), indicating an energetically heterogeneous surface.[49]

The maximum adsorption uptake at 100 kPa is comparable to other MOFs previously reported under relatively similar conditions. For example, Zarate *et al.* have studied the adsorption properties of MIL-53(Al)-NH_2 under 1 bar at 283 K and measured a capacity of 1.6 mmol g^{-1}.[50] Shekhah *et al.* reported a capacity of 2.3 mmol g^{-1} under 1 bar at 308 K for SIFSIX-3-Zn.[51] Grajciar *et al.*[52] measured a capacity at a saturation of 13 mmol g^{-1} under 15 bar at 303 K for Cu-BTC. Zhao *et al.* reported CO_2 adsorption capacities for JUC-141 one order of magnitude higher compared to this study.[15] It should be noted that a lower CO_2 uptake should be considered as the result of a more disordered structure, which is expected for samples obtained *via* rapid microwave assisted solvothermal synthesis. A lower adsorption capacity in our studies when the activation is carried out at 493 K can be attributed to the highly flexible layered structure of this MOF and the easy generation of slit-shaped mesopores and larger macropores upon thermally-induced ligand detachment from the metal centre and the introduction of Cu(I) defects in the structure. We also observe that the degassing pressure used in the activation process has a

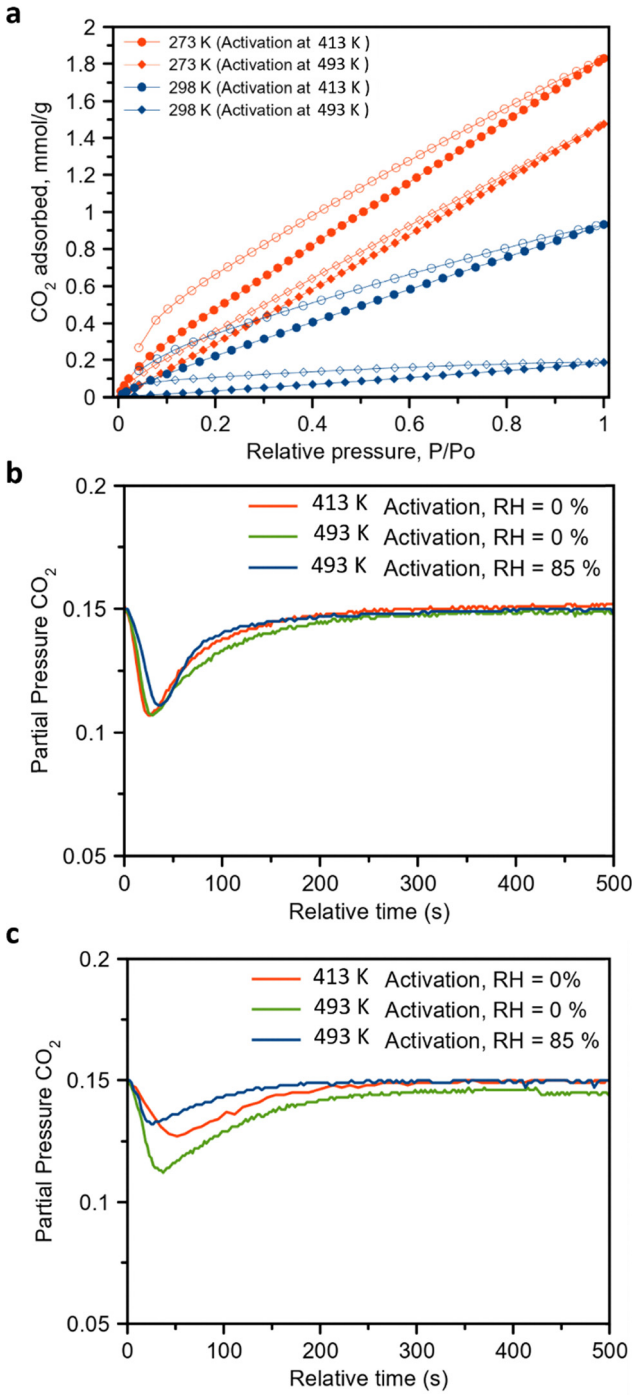

Fig. 4 (a) CO_2 adsorption isotherms of Cu-1 at different temperatures as indicated after applying different degassing conditions and a pressure of 0.1 Pa. (b) CO_2 breakthrough experiments at 273 K after applying different activation conditions as indicated; and (c) CO_2 breakthrough experiments at 298 K after applying different activation conditions as indicated.

strong influence on the final adsorption capacity where a higher pressure of 1 Pa, amongst other factors, yielded a much lower CO_2 uptake of 0.4 mmol g^{-1} (Fig. S10a, ESI†).

This is consistent with TG, XRD (Fig. S11, ESI†) and N_2 adsorption isotherm analysis after CO_2 adsorption experiments (Fig. S12a and b, ESI†) and after degassing at 473 K and 1 Pa for longer time 12 hours (Fig. S12c, ESI†), showing that the structure is globally preserved although the specific surface area decreases due to a change in the 3D network of H-bonds induced by the thermal treatment and the evacuation process during the activation leading to an increase of the macroporosity. Nevertheless, in terms of selectivity, the GCMC simulations, presented later on, predict high enthalpies in the presence of defective sites, which makes this material a potentially interesting candidate for the separation of gas mixtures. This is hypothesised based on the generation of open Cu sites as well as Cu(I) defective sites. Consequently, we study the capture properties of these materials for CO_2 in a simulated CO_2/N_2 gas mixture at ambient pressure. The breakthrough curves at 273 K and 298 K are reported in Fig. 4b and c, respectively. The amount of CO_2 adsorbed from a 15 : 85, CO_2 : N_2 mixture at 273 K amounts to 0.62 mmol g^{-1} when the activation of Cu-1 is carried out at 493 K and to 0.41 mmol g^{-1} for activation at 413 K, indicating the beneficial effect of the higher degassing temperature on the formation of selective sites for CO_2 capture, despite the overall specific surface area being decreased. The adsorption capacity for a simulated mixture is significantly reduced when the CO_2 is adsorbed at room temperature. At 298 K, the amount of CO_2 adsorbed from the mixture significantly decreases to 0.17 mmol g^{-1} for degassing at 493 K and to 0.09 mmol g^{-1} for degassing at 413 K. One could postulate that the remaining sites are the portion of highly selective sites for CO_2 capture.

The presence of water molecules (relative humidity 85%) is however detrimental, leading to a significant decrease of CO_2 adsorbed amounting to 0.4 mmol g^{-1} and 0.05 mmol g^{-1} at 273 K and 298 K, respectively. Consequently, despite the sufficiently good affinity for CO_2 capture, the presence of water limits the applicability of these systems for selective capture.

3.3.2. *In situ* soft and hard X-ray spectroscopy. To investigate the nature of the highly selective sites for CO_2, we applied *in situ* spectroscopy over Cu-1. We first discuss the surface sensitive NEXAFS study (Fig. 5). It must be pointed out that during the *in situ* measurements at the ISISS beamline at BESSY II, the sample suffered beam damage upon prolonged irradiation and under UHV conditions, consisting of the reduction of the Cu(II) to Cu(I) (Fig. S13a, ESI†). At the same time the intensity of the resonance at 532 eV in the O K-edge spectrum decreased, which was assigned to the 1s → π* O 2p–Cu 3d resonance. At the same time, the resonance attributed to C–O species increases, consistent with the detachment of a carboxylate ligand from the Cu site (Fig. S13, ESI†). However, such a defect is generally found in Cu-MOFs systems containing Cu paddle wheels, such as H-KUST-1,[18] but more so in the Cu(AIPA) monoclinic structure. It is safe to state that the measurement presented in Fig. 3d as well as in Fig. S13 (ESI†) (scan-1) is well representative of the natural abundance of these defects in the Cu-1 MOF synthesised in this work, whereas a longer exposure would lead to the photon-induced formation of the Cu(I) sites. The evolution of the Cu L-edge in UHV (10^{-7} mbar) and under a CO_2 atmosphere as indicated in

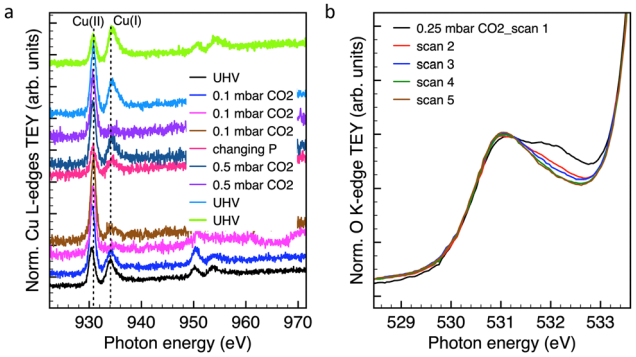

Fig. 5 NEXAFS spectra measured for Cu-1 under CO_2 pressure in the millibar range as indicated: (a) Cu L-edges (order of the experiments from bottom to top) and (b) O K edge.

Fig. 5 shows that CO_2 chemisorbs on the Cu(I) sites re-oxidizing them to Cu(II). This suggests that CO_2 coordinates *via* the oxygen atom to Cu. The time resolved O K-edge measurements on the same spot under 0.25 mbar CO_2 indicate a chemisorbed CO_2 state at 532 eV, which suffers beam damage with time (Fig. 5b). This resonance is found at the same photon energy as the species desorbing due to beam damage in UHV suggesting for a Cu–O species (Fig. S13, ESI†). No significant changes were observed in the C K-edge (not shown). The experiments proved that CO_2 adsorbs on exposed Cu sites *via* the O atom. This is consistent with earlier work on the defect sites of the HKUST-1.[18]

The soft X-ray *in situ* study on Cu-2 did not show any dynamic changes at the Cu L-edges in both TEY and EY (not shown), the first slightly more bulk sensitive than partial Auger electron yield (EY), indicating the detrimental effect of the impurity phases (Fig. 2d). An explanation for this finding is that: (i) the nanostructures deposited on the surface covering the large particle are not involved in the CO_2 adsorption and are detrimental by preventing CO_2 access into the pores and (ii) the low abundance of Cu(I) sites for this sample. We performed an additional *operando* study on the Cu-1 at the I14 beamline at DLS by means of hard X-ray spectromicroscopy at the Cu K-edge with the goal to have information about the localization of the CO_2 adsorption process. These data are reported in the ESI† in Fig. S14. Here, XANES maps are obtained under *in situ* conditions: first the sample is measured at room temperature while flowing N_2, then at 473 K in N_2 and lastly at room temperature while flowing CO_2. Each of these maps was taken in a different area on the sample, but with some overlap between all three maps (Fig. S14a, ESI†). Principal component analysis was then used to identify clusters of XANES spectra, which are similar in shape and thus have a similar chemical composition (Fig. S14b, ESI†).

Accordingly, we can observe that the sample is composed of a mixture of Cu(I)/Cu(II) in N_2 at room temperature (Fig. S14c, ESI†). To study differences in the ratio of Cu(I) to Cu(II) upon changes in the *in situ* conditions, we study the absorption intensity at the pre-edge peak with respect to the edge (I_{pe} = intensity pre-edge/intensity edge × 100) rather than performing a fit of reference compounds. This is the preferred method due to a lack of suitable reference samples that would be required for fitting the full spectra. For the initial sample conditions I_{pe}= 38% for the bulk of the sample, and I_{pe} = 40% for the edge.

Next a thermal treatment up to 473 K in N_2 flow was performed to remove the DMF as found by TG analysis (Fig. S11a, ESI†). Under this condition, we can see no changes in the particle shape, whereas the I_{pe} increases to 75% of the edge intensity and the pre-edge peak moves to slightly higher energy (8980.6 eV to 8982.1 eV), indicating a change in copper speciation and/or the coordination environment of the Cu atoms. This process seems slightly more pronounced in the bulk than in the edge of the sample, where I_{pe} only rises to 71%. The increase in I_{pe} indicates an increase of Cu(I) abundance, corresponding to the formation of uncoordinated defective sites, but the energy shift would contradict this and instead indicate an increase in Cu(II). Therefore, we conclude that in addition to a speciation change the coordination environment of the Cu atoms is changed, affecting the spectral shape. This could be caused by the removal of DMF, as organic solvents can change the shape of the XANES spectrum[53] or potentially by changes in the porosity of the material or the detachment of one of the ligands during thermal annealing. Possible effects from thermal degradation are further discussed below. Notably, by cooling down to RT and feeding CO_2, we observe a decrease in the pre-edge peak (I_{pe} = 67% for the bulk, I_{pe} = 66% for the edge), which indicates a reduction of the Cu(I) resonance, consistent with the soft X-ray data. Whilst we were able to capture these dynamics, some thermal degradation of the sample at 473 K could be expected together with the possibility that the fluid dynamic conditions realized in the *in situ* cell limit the diffusion of the CO_2 into the framework. Furthermore, effects of beam radiation are observed in the XRF image (Fig. S14a, ESI†); thus, a study of the influence of the X-ray beam on the XANES spectra is required.

To investigate the effect of beam damage on the hard X-ray XANES spectra, we obtained point-XANES measurements (Fig. S15, ESI†). First, a scan was taken with 10 milliseconds per energy step dwell time (scan 0), corresponding to the dwell time used to obtain the XANES maps in Fig. S14 (ESI†). Next, another scan was taken in a different position at 100 milliseconds per energy step dwell time (scan 1), corresponding to a 10× higher beam exposure than was used to obtain the XANES maps. A total of 4 consecutive scans were taken in this position, to investigate changes in the spectral shape upon repeated beam exposure. The mapped XANES spectra discussed before were the result of an average from each region, where each individual pixel contains one spectrum. In contrast, for the point XANES performed here, with a focused (50 nm) beam (Fig. S15, ESI†), this averaging cannot be performed, resulting in significantly increased noise levels in the spectra in the post-edge region (Fig. S15b, ESI†). This complicates normalization of the spectra, making a direct comparison of the full spectral shape of the various scans difficult. As such, we instead use the ratio between the intensity of the pre-edge peak and the absorption edge prior to normalization (I_{pe}). The results give

I_{pe} = 37% for scan 0 and I_{pe} = 35% for scan 1. This indicates that during a single XANES scan beam damage does not significantly alter the shape of the absorption edge region regardless of dwell time, even if beam effects can be observed after the full scan is completed in corresponding XRF images (Fig. S15a, ESI†). This can be understood in that the scans are performed from low to high energy levels and beam effects will be strongest at energies that are equal to or higher than the absorption edge. In concurrence with this, when consecutive scans were taken in the same position as scan 1, I_{pe} rises to 47% or 48%, indicating that beam damage does play a role when repeatedly measuring the same area. As such, this raises questions on the reliability of the 473 K N_2 and RT CO_2 scans. However, it should be considered that point XANES measures continuously in one area, while XANES maps scan in a raster, allowing time for beam effects (such as local sample heating) to dissipate between scans. Additionally, consecutive scans here are performed at 10× the dwell time used in the XANES maps. The maps are also taken in different areas, with some overlap between all. This did not give additional clusters for the measured and unmeasured area, so we conclude that the spectra are unaffected by the beam.

In addition to beam damage effects, Cu MOFs can degrade when exposed to high temperatures for prolonged periods of time. This can further affect the shape of the XANES scan.[54] The single point CO_2 isotherms in Fig. 4 show that for the degassing at 0.1 Pa, the amount of CO_2 adsorbed by Cu-1 is higher when the degassing is performed at 413 K compared to 493 K, which is a clear indication of a loss of exposed surface area and porosity due to a thermal induced partial structural degradation. As the XANES scan at 473 K takes 2 hours and 45 minutes to complete, this effect can be expected to occur during this measurement. Since the XANES scans were taken from low to high energy levels, the absorption edge of the 473 K measurement is reached after keeping the sample at this temperature for 1 hour, so that the comparison between edge and pre-edge peak intensity should remains valid. However, it can be expected that the spectral shape in the RT CO_2 measurement is affected compared to the previous scans. This complicates any quantitative analysis of the spectra, but an increase in Cu(II) abundance is still apparent regardless of the formation of Cu(I) sites during thermal annealing.

We show here a reduction of Cu(II) to Cu(I) during heat treatment that is slightly more pronounced in the bulk of the sample compared to the edges. We also observe a subsequent oxidation back to Cu(II) upon CO_2 capture. However, careful consideration is required with regard to thermal degradation of the sample, which can affect the spectral shape and therefore limits the analysis to qualitative rather than quantitative interpretation.

3.3.3. Simulated isotherm by the GCMC approach. The comparative analysis of how the degassing temperature affects both the single-point and dynamic CO_2 adsorption properties has identified the presence of CO_2-selective sites, although the structure is unstable when water is present. GCMC is used to simulate the adsorption isotherms as a strategy to identify the molecular level characteristics of these sites. The predicted isotherms are compared with the experimental data in Fig. 6. To emphasize the effect of the new possible sites generated by the microwave-assisted synthesis developed in this study as well as by the degassing conditions in the activation treatment, the simulated isotherm of a defect-free model was also included. Unlike the simulated isotherm of defect-free monoclinic Cu(AIPA), the experimental isotherms do not show a steep increase of adsorption at lower partial pressure, typical of microporous materials, followed by a plateau with increasing pressure indicative of isoenergetic sorption sites within size-homogeneous pores. Instead, the experimental isotherms present a monotonic increase in CO_2 adsorption with increasing partial pressure, ultimately surpassing the uptake of the defect-free system. This behavior is attributed to the heterogeneous nature of the defects sites and their location within the highly flexible framework of the MOF as described in section 3.2, highlighting the impact of new spaces resulting from the removal of ligands (see Fig. S1b, g, h and i, ESI†). Three defect models were evaluated, each with varying concentrations of Tri-Cu(I), Di-Cu(I), and Tetra-Cu(II) sites. The best agreement with the experimental isotherms was achieved by two models, namely defective model 1 and defective model 2. The former corresponds to 30% of Tri-Cu(I) 5% of Di-Cu(I) and 65% of Tetra-Cu(II) and the latter to 35% of Tri-Cu(I) 10% of Di-Cu(I) and 55% of Tetra-Cu(II). These models provide valuable insight into the microscopic mechanisms governing the adsorption process. Notably, under higher degassing pressure (1 Pa), the CO_2 adsorption isotherms of Cu-1 are well described by a specific composition of Tetra-Cu(II) and Tri-Cu(I) defects alone (Fig. S10b, ESI†), suggesting that Di-Cu(I) sites arise only under harsher degassing conditions, which in turn enhance CO_2 selectivity.

A slight discrepancy is observed between the theoretical and experimental isotherms (see Fig. 6), which could arise from several factors: (i) a minor deviation in defect concentration;

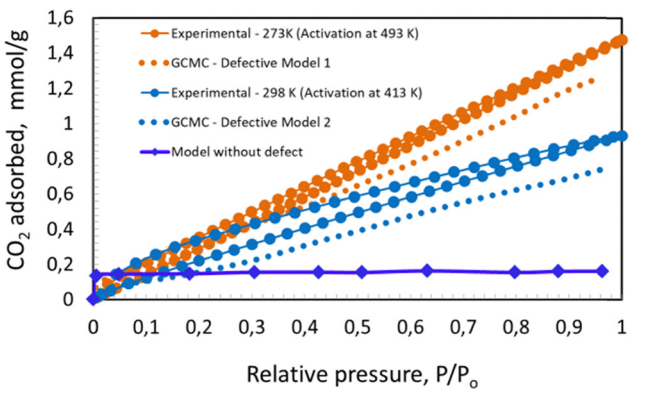

Fig. 6 Comparison between GCMC adsorption isotherms determined at different defects and the experimental CO_2 adsorption isotherms of Cu-1 carried out at different degassing conditions. Defective model 1 corresponds to 30% of Tri-Cu(I) and 65% of Tetra Cu(II) and 5% of Di-Cu(I) and the defective model 2 corresponds to 35% of Tri-Cu(I) and 55% of tetra Cu(II) and 10% of Di-Cu(I).

(ii) limitations in the Cu-1 model, which assumes homogeneous defect distribution, whereas defect interactions may actually lead to a non-uniform distribution; (iii) inaccuracies in the force field parameters used; and (iv) limitations in the qEq approach for calculating the partial charges in the Cu-1 structure. These factors may contribute to minor inaccuracies and a slightly lower predicted adsorption capacity at saturation. Nonetheless, the good overall agreement between the experimentally measured and simulated isotherms provides sufficient confidence to infer key parameters that govern CO_2 adsorption and its microscopic mechanism. We specifically examined the adsorption isotherm at low pressures and at saturation to gain insight into possible CO_2 adsorption mechanisms at the microscopic level.

To examine the interactions at low pressure, we isolated and optimized three clusters containing the defective sites in each cluster (see Fig. S1d–f and S16a, c, e, ESI†) and used the adsorption locator approach based on the simulated annealing algorithm for locating CO_2, H_2O and N_2 within each cluster.[55,56] Analysis of these calculations shows clearly that the CO_2 molecule is adsorbed in the order: Di-Cu(I) > Tri-Cu(I) > Tetra-Cu(II). The calculations indicated different adsorption energies for the different defective sites: −80 kJ mol^{-1}, corresponding to the Di-Cu(I) site, −75 kJ mol^{-1}, corresponding to the Tri-Cu(I) site and −31.5 kJ mol^{-1}, corresponding to the Tetra-Cu(II) site, with the calculated Cu–O bond lengths of 1.90 Å, 2.15 Å and 2.75 Å, respectively (Fig. 7). The adsorption energy of CO_2 at the Di-Cu(I) sites is more than twice that of Tri-Cu(II) and Tetra-Cu(II) sites. The CO_2 adsorption enthalpy was investigated by Liang *et al.*[57] for Cu-BTC (H-KUST-1), which contains the same copper paddle wheels. In their study, the enthalpy of adsorption determined directly by differential thermal analysis (DTA) was −30 kJ mol^{-1}, consistent with our calculated value for the case of the Tetra-Cu(II) site. However, their work did not specify the nature of the sites where the CO_2 molecules were adsorbed. Grajciar *et al.*[52] studied CO_2 adsorption in a Cu-BTC MOF by using DFT calculations and compared the results with microcalorimetry. They reported a heat of adsorption of −29 kJ mol^{-1} obtained experimentally and −29.1 kJ mol^{-1} calculated by the DFT method. In their theoretical model, they considered a very low loading of CO_2 molecules, which are physisorbed on the Tetra-Cu(II) site. However, the values of the adsorption energies of a CO_2 molecule in the cases of Di-Cu(I) and Tri-Cu(I) sites are 80 kJ mol^{-1} and 75 kJ mol^{-1}, which can be considered as chemisorption. These relatively high heats of adsorption in the case of the Di-Cu(I) and Tri-Cu(I) defective sites can be attributed to a sterically favorable electrostatic interaction with CO_2. Therefore we calculated the partial charges, which are 1.6 for q(Di-Cu(I)), 2.74 for q(Tri-Cu(I)), and 3.13 for q(Tetra-Cu(II)). The lower positive charge indicates that the copper contains higher electron density and might contribute to a stronger π-back donation from the orbitals of the metal ion to the orbitals of the CO_2 molecule.[58] Su *et al.*[59] also demonstrated that the back-bonding interactions between metal orbitals and antibonding orbitals of small molecule guests promote the chemisorption process. Although the calculated adsorption energies do not explicitly account for π-back donation, which was shown to occur in Cu-(II)-paddle wheel MOFs,[58] our results confirm that steric hindrance, site-specific interactions and lateral electrostatic effects play a significant role in influencing adsorption behaviour. These factors collectively affect the binding affinity and orientation of CO_2 at the adsorption sites, underscoring the complexity of adsorption mechanisms. The predicted enthalpy of adsorption for CO_2 interacting with a MOF containing copper metal, calculated using the GCMC approach, range from 29 to 75 kJ mol^{-1}, while the experimentally measured enthalpy is calculated to be between 25 and 40 kJ mol^{-1}.

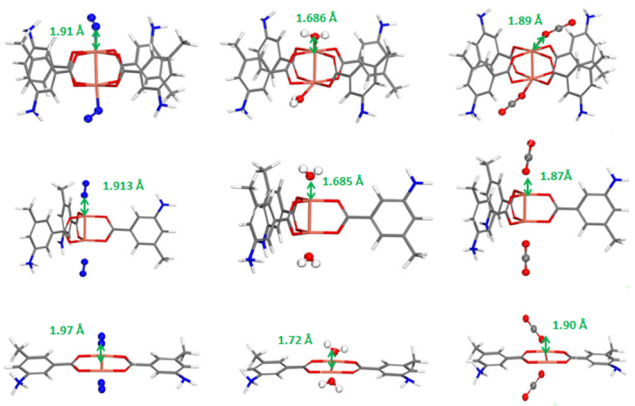

Fig. 7 The single CO_2, N_2 and H_2O adsorbed on the defective sites, at low loading.

This discrepancy between the theoretical predictions and experimental results can be reasonably explained by considering the limitations of the GCMC approach and thermodynamic factors. The GCMC approach is a powerful simulation technique widely used for modeling adsorption processes in porous materials. However, it has some inherent limitations that may affect the accuracy of the predicted adsorption enthalpies likely due to force field limitations, and the treatment of defects. The adsorption enthalpy reflects the overall energy change when CO_2 molecules interact with the Cu-MOF surface. Several factors can influence the difference between the predicted and experimental values. Experimentally, the enthalpy of adsorption is often determined as an average over multiple adsorption sites, including both strong and weak binding locations. The experimentally measured range (25–40 kJ mol^{-1}) probably reflects a combination of various adsorption sites, including those at defect-free and defect-containing regions (see Fig. S9, ESI†). The broader range predicted by GCMC (30–75 kJ mol^{-1}) may indicate that the simulation captures stronger interactions at specific defect sites, while less accurately representing the weaker interactions. The actual concentration and distribution of defects in the Cu-MOF can vary, affecting the average adsorption strength. If the GCMC simulations assume a higher number of defect sites than that is present experimentally, then this may lead to overestimated enthalpies. In contrast, experimental samples that might have a more diverse range of local environments result in a lower observed average. Our calculated

values are consistent with the observations of Drenchev *et al.*,[60] who studied open metal sites in the organic framework CPO-27-Cu (Cu MOF 74), containing a paddlewheel unit, which is structurally similar to the Cu-MOF, and deduced from IR spectroscopy an enthalpy of adsorption of about 63 kJ mol^{-1} for a CO_2 molecule specifically adsorbed on the Tri-Cu(I) site, and approximately 20 kJ mol^{-1} on the Tetra-Cu(II) site. Itadani *et al.*[61] studied the coordinative unsaturated Cu(I) sites in the MFI zeolite and found high isosteric heats in the range of 50–130 kJ mol^{-1} for CO_2 molecules. The most probable arrangements of CO_2 were further investigated by GCMC simulations under saturation conditions and the main adsorption sites were extracted (see Fig. S17a–e, ESI†). It can be seen that the simulated isotherm reproduces well the experimental data, corroborating the validity of the microscopic models of the CO_2 adsorption mechanism. An in-depth analysis of the snapshots at saturation allowed us to gain more insight into the configurations of the adsorbed molecules. In the case of the Tetra-Cu(II) site, the CO_2 molecule is oriented with the O atoms pointing towards the Cu(II) ion of the framework at an average distance of 3.00 Å from the Tetra-Cu(II) and of 3.45 Å from the O atom of an adjacent CO_2 molecule in closest proximity. In the case of the Tri-Cu(I) site, the CO_2 molecule interacts *via* its O atoms with Cu(I) ion with a mean separating distance of 1.97 Å; the nearest CO_2 molecule is located 3.54 Å away (intermolecular O–O distance). In the case of the Di-Cu(I) site, the CO_2 molecule interacts *via* its O atoms with Cu(I) ion with a mean separating distance of 1.83 Å. That site has the potential to be the most favourable for CO_2 adsorption. We also found a new adsorption site for CO_2 molecules at saturation, which is the interaction between CO_2 molecules and the $-NH_2$ group (see Fig. S17c, ESI†), and the $-NH_3^+$ group (see Fig. S17e, ESI†) whereas, at low pressure, location at this site has not been observed. The calculated intermolecular O–H hydrogen bond length is 2.34 Å and 2.026 Å, between NH_2–CO_2 and NH_3^+–CO_2, respectively, indicating that the interaction between the adsorbed CO_2 molecule and the $-NH_3^+$ and $-NH_2$ groups actively contributes to the process of adsorption of CO_2. We suggest that the adsorption of the CO_2 molecule on the $-NH_2$ and $-NH_3^+$ groups can take place only when the coordinative unsaturated Cu sites are fully saturated by CO_2 adsorption.

The GCMC simulations conducted in this study reveal that under-coordinated open metal sites create unique adsorption environments that increase the affinity and selectivity of the material for certain gas molecules. In the context of gas separation, tuning the concentration of such under-coordinated Cu(I) sites could by modulating the synthesis conditions provide a powerful tool for tailoring the selectivity of Cu-MOF materials towards CO_2 capture from flue gas streams or natural gas purification. Defect engineering, such as deliberate introduction of structural vacancies or alterations in linker types, may further promote the formation of low-coordination metal sites, thus enhancing the tunable adsorption properties. The GCMC simulations were conducted on Cu-MOF structural models to evaluate the adsorption properties of CO_2/N_2 mixtures at a 15 : 85 ratio. This specific gas mixture composition was chosen to mimic typical conditions encountered in gas separation processes, where the selective capture of CO_2 from nitrogen-rich mixtures is critical for applications such as carbon capture and flue gas purification. The simulations were designed to assess the MOF's inherent selectivity for CO_2 over N_2 and to understand the role of specific structural features of the MOF in governing this behavior. To further investigate the impact of water on adsorption performance, the study extended the analysis to ternary mixtures by introducing H_2O alongside CO_2 and N_2. The presence of H_2O in the adsorption environment is highly relevant for real-world applications, as many industrial gas streams contain significant water content. Water molecules can compete with CO_2 and N_2 for adsorption sites, potentially altering the selectivity profile of the MOF and affecting the efficiency of gas separation processes. Therefore, a comparison was made between the binary mixture data for CO_2/N_2 (15 : 85) and the ternary mixture data for $CO_2/N_2/H_2O$ to elucidate the influence of water on the selective adsorption characteristics of the Cu-MOF (Table 3).

Table 3 The performance of the N_2/CO_2 mixture in terms of IAST selectivity compared to the $N_2/CO_2/H_2O$ mixture predicted at 228 K under 1 bar

Cu-MOFs	Pressure (bar)	Temperature (K)	IAST selectivity of CO_2/N_2 (15 : 85)	IAST selectivity of $CO_2/N_2/H_2O$
Defective model 1	1	298	13	0.8
Defective model 2	1	298	9	0.5

The selectivity of the two structural models was evaluated at 298 K and 1 bar. The defective model 1, with a composition of 30% Tri-Cu(I), 65% tetra Cu(II), and 5% Di-Cu(I), exhibited a selectivity of 13. In contrast, defective model 2, consisting of 35% Tri-Cu(I), 55% Tetra-Cu(II), and 10% Di-Cu(I), showed a selectivity of 9. These results suggest that the selectivity is primarily governed by the chemical environment of the Cu sites in the Cu(AIPA), rather than by porosity, which appears to have an insignificant impact. As illustrated in Fig. 7, the CO_2 molecules exhibit a stronger affinity for the Cu-MOF sites compared to N_2, as evidenced by shorter intermolecular distances between CO_2 and the Cu sites. However, the calculated enthalpy of adsorption for N_2 molecules shows higher values at certain defect sites: -120 kJ mol^{-1} for the Di-Cu(I) site, -25 kJ mol^{-1} for the Tri-Cu(I) site and -160 kJ mol^{-1} for the Tetra-Cu(II) site. This apparent discrepancy arises because enthalpy values represent the energy released during adsorption but do not account for the spatial arrangement or the frequency of favorable interactions across the system. While N_2 shows higher adsorption enthalpies at specific sites, these sites are less accessible compared to those favoring CO_2 adsorption, resulting in lower overall selectivity for N_2. CO_2 has unique molecular properties, such as its linear structure and significant quadrupole moment, allowing it to engage in stronger and more directional interactions with unsaturated copper sites. These are dominated by electrostatic and Lewis acid–base interactions, leading to CO_2 being localized closer to the copper

centers. In contrast, N_2, with its weaker quadrupole moment and less directional interactions, requires more energy to adsorb at certain high-energy sites but does not achieve the same proximity as CO_2. The higher enthalpy values for N_2 adsorption can also be attributed to the limitations of the GCMC approach, which, while valuable for modeling adsorption processes, is less suited for predicting accurate adsorption enthalpies. GCMC relies on empirical force fields that cannot fully capture electronic effects such as orbital overlap or charge transfer, which are essential for understanding the chemical nature of gas-MOF interactions. In contrast, density functional theory (DFT) provides site-specific adsorption energies and accounts for these effects, offering a more precise understanding of adsorption and energetic mechanisms. Therefore complementary DFT studies might enable to achieve a more accurate depiction of the adsorption and energetic processes at play.

Notably, the most favorable site for N_2 adsorption is the Tri-Cu(I) site. However, the overall preferential adsorption of CO_2 arises from its ability to interact more effectively with a broader range of sites, emphasizing the Cu-MOF inherent selectivity for CO_2 over N_2.

The 'defect1' model exhibits a notable abundance of Tri-Cu(I) sites, significantly enhancing its selectivity toward N_2. When simulating N_2/CO_2 separation in the presence of water, both models showed a drastic reduction in selectivity, decreasing by a factor of 10. The results, summarized in Table 3, reveal clear differences in selectivity when H_2O is introduced into the system. CO_2/N_2 selectivity decreases significantly in the presence of water, indicating that H_2O molecules have a strong affinity for the adsorption sites within the Cu-MOF framework. This effect is probably due to the polar nature of water, which enables it to interact strongly with the metal centers and other polar sites within the MOF. These interactions can occur through strong hydrogen bonding with under-coordinated metal sites (see Fig. 7), which may preferentially bind H_2O over CO_2 or N_2. Consequently, the CO_2 adsorption capacity is reduced in the ternary mixture, as water occupies critical adsorption sites, thereby impacting the overall gas separation efficiency. The results highlight the need to consider the effects of water in practical applications, as the presence of water can reduce CO_2 capture efficiency and selectivity.

4. Conclusions

In this study, we have presented a comprehensive investigation into the synthesis and characterization of a Cu-MOF with a monoclinic Cu(AIPA) structure, synthesized *via* a rapid microwave-assisted solvothermal method. Our results demonstrate that precise control over the ligand-to-metal precursor ratio and heating profile enables the formation of a phase-pure material enriched with coordinatively unsaturated Cu(I) defect sites. These sites have been shown—through a combination of *in situ* and *operando* spectroscopy, adsorption isotherms, and GCMC simulations—to play a pivotal role in enhancing CO_2 capture performance.

The good agreement between experimental and computational data confirms that the presence of Cu(I) defects significantly improves CO_2 adsorption capacity compared to defect-free analogues. Importantly, the ability to induce and tune these defects through rapid synthesis and post-synthetic thermal treatment offers a scalable and energy-efficient alternative to conventional solvothermal methods, with direct implications for industrial gas separation technologies. However, the presence of water remains a critical challenge, as it competes for adsorption sites and diminishes CO_2 selectivity, besides causing structural degradation. This highlights the urgent need for the development of water-tolerant MOF systems. Future work should focus on engineering MOF-based composites and implementing strategies to mitigate water interference, thereby preserving high CO_2 selectivity under humid conditions. These advancements will be essential for translating MOF-based materials into viable solutions for real-world carbon capture and gas purification applications.

Author contributions

The manuscript was written through contributions of all authors. All authors have given approval to the final version of the manuscript.

Conflicts of interest

There are no conflicts to declare.

Data availability

Data for this article are available at the Salford repository: www.**https://worktribe.com**.

Acknowledgements

The research leading to the *in situ* soft X-ray spectroscopic results has been supported by the project CALIPSOplus under Grant Agreement 730872 from the EU Framework Program for Research and Innovation HORIZON 2020. Computing facilities for this work were provided by ARCCA at Cardiff University, HPC Wales, and through our membership of the U.K.'s Materials Chemistry Consortium (MCC). This work also used the Cirrus UK National Tier-2 HPC Service at EPCC (**https://www.cirrus.ac.uk**) funded by the University of Edinburgh and EPSRC (EP/P020267/1). *In situ* soft X-ray spectroscopic measurements were carried out at the ISISS beamline at Helmholtz-Zentrum Berlin für Materialien und Energie. We thank HZB for the allocation of synchrotron radiation beamtime under the proposal ST 18106826. We thank DLS for the allocation of beamtime under the proposal SP28630 and SI32308. The UK Catalysis Hub is thanked for resources and support provided *via* our membership of the UK Catalysis Hub Consortium and funded by EPSRC grants: EP/R026939/1, EP/R026815/1, EP/R026645/1, EP/R027129/1 or EP/M013219/1.

Notes and references

1 M. Mikkelsen, F. C. Krebs and M. Jørgensen, *Energy Environ. Sci.*, 2010, **3**, 43–81.
2 R. Lindsey, **https://Climate.gov**, 2020, Available at: **https://www.climate.gov/news-features/understanding-climate/climate-change-atmospheric-carbon-dioxide**.
3 G. Centi, S. Perathoner, C. Genovese and R. Arrigo, *Chem. Commun.*, 2023, **59**, 3005–3023.
4 E. S. Sanz-Pérez, C. W. Jones, S. A. Didas and C. R. Murdock, *Chem. Rev.*, 2016, **116**, 11840–11876.
5 D. M. D'Alessandro, B. Smit and J. R. Long, *Angew. Chem., Int. Ed.*, 2010, **49**, 6058–6082.
6 G. Sneddon, A. Greenaway and H. H. P. Yiu, *Adv. Energy Mater.*, 2014, **4**, 1–19.
7 H. Furukawa, K. E. Cordova, M. O'Keeffe and O. M. Yaghi, *Science*, 2013, **341**, 80.
8 N. L. Rosi, J. Eckert, M. Eddaoudi, D. T. Vodak, J. Kim, M. O' Keeffe and O. M. Yaghi, *Science*, 2014, **300**, 1127–1129.
9 M. Ding, X. Cai and H. L. Jiang, *Chem. Sci.*, 2019, **10**, 10209–10230.
10 (*a*) R. Sanz, F. Martínez, G. Orcajo, L. Wojtas and D. Briones, *Dalton Trans.*, 2013, **42**, 2392–2398; (*b*) M. T. Kapelewski, S. J. Geier, M. R. Hudson, D. Stück, J. A. Mason, J. N. Nelson, D. J. Xiao, Z. Hulvey, E. Gilmour, S. A. FitzGerald, M. Head-Gordon, C. M. Brown and J. R. Long, *J. Am. Chem. Soc.*, 2014, **136**(34), 12119; (*c*) D. E. Jaramillo, D. A. Reed and H. Z. H. Jiang, *et al.*, *Nat. Mater.*, 2020, **19**, 517–521.
11 Y. Zhao, M. Seredych, J. Jagiello, Q. Zhong and T. J. Bandosz, *Chem. Eng. J.*, 2014, **239**, 399–407.
12 S. Bordiga, L. Regli, F. Bonino, E. Groppo, C. Lamberti, B. Xiao, P. S. Wheatley, R. E. Morris and A. Zecchina, *Phys. Chem. Chem. Phys.*, 2007, **9**, 2676–2685.
13 (*a*) J. Szanyi, M. Daturi, G. Clet, D. R. Baerc and C. H. F. Pedena, *Phys. Chem. Chem. Phys.*, 2012, **14**, 4383–4390; (*b*) P. St. Petkov, G. N. Vayssilov, J. Liu, O. Shekhah, Y. Wang, C. Wöll and T. Heine, *ChemPhysChem*, 2012, **13**, 2025–2029.
14 (*a*) W. Zhao, Z. Zhang, Z. Li and N. Cai, *Ind. Eng. Chem. Res.*, 2013, **52**, 2084–2093; (*b*) M. W. Hahn, *et al.*, *J. Phys. Chem. B*, 2016, **120**, 1988–1995; (*c*) H. R. Mahdipoor, R. Halladj, E. Ganji Babakhani, S. Amjad-Iranagh and J. Sadeghzadeh Ahari, *RSC Adv.*, 2021, **11**, 5192–5203; (*d*) J. Sun, Z. Yi, X. Zhao, Y. Zhou and C. Gao, *RSC Adv.*, 2017, **7**, 14678–14687; (*e*) A. C. Forse, P. J. Milner, J.-H. Lee, H. N. Redfearn, J. Oktawiec, R. L. Siegelman, J. D. Martell, B. Dinakar, L. B. Zasada, M. I. Gonzalez, J. B. Neaton, J. R. Long and J. A. Reimer, *J. Am. Chem. Soc.*, 2018, **140**(51), 18016–18031.
15 N. Zhao, F. Sun, P. Li, X. Mu and G. Zhu, *Inorg. Chem.*, 2017, **56**(12), 6938–6942.
16 W. Q. Xu, *et al.*, *Inorg. Chem. Commun.*, 2018, **92**, 1–4.
17 T. Ahnfeldt, *et al.*, *Angew. Chem.*, 2009, **121**, 5265–5268.
18 L. Braglia, *et al.*, *J. Phys. Chem. Lett.*, 2021, **12**, 9182–9187.
19 L. Zhao, *et al.*, *J. Mol. Model.*, 2011, **17**, 227–234.
20 L. Boudjema, *et al.*, *Inorg. Chim. Acta*, 2020, **501**, 119316.
21 S. Kojima, *et al.*, *SSRN Electron. J.*, 2022, 1–35.
22 D. Dubbeldam, K. S. Walton, D. E. Ellis and R. Q. Snurr, *Angew. Chem.*, 2007, **119**, 4580–4583.
23 (*a*) A. J. O'Malley and C. R. A. Catlow, *Phys. Chem. Chem. Phys.*, 2013, **15**, 19024–19030; (*b*) T. Khuong Trung, P. Trens, N. Tanchoux, S. Bourrelly, P. L. Llewellyn, S. Loera-Serna, C. Serre, T. Loiseau, F. Fajula and G. Ferey, *J. Am. Chem. Soc.*, 2008, **130**, 16926–16932; (*c*) C. Mellot-Draznieks, C. Serre, S. Surblé, N. Audebrand and G. Férey, *J. Am. Chem. Soc.*, 2005, **127**, 16273–16278.
24 K. Sladekova, *et al.*, *Adsorption*, 2020, **26**, 663–685.
25 D. Dokur and S. Keskin, *Ind. Eng. Chem. Res.*, 2018, **57**, 2298–2309.
26 M. Agrawal and D. S. Sholl, *ACS Appl. Mater. Interfaces*, 2019, **11**, 31060–31068.
27 S. Caro-Ortiz, E. Zuidema, M. Rigutto, D. Dubbeldam and T. J. H. Vlugt, *J. Phys. Chem. C*, 2020, **124**, 24488–24499.
28 A. V. Brukhno, *et al.*, *Mol. Simul.*, 2021, **47**, 131–151.
29 A. Aguado and P. A. Madden, *J. Chem. Phys.*, 2003, **119**, 7471–7483.
30 K. Binder and D. W. Heermann, *Theoretical Foundations of the Monte Carlo Method and Its Applications in Statistical Physics*, Springer, 1992, pp. 5–67.
31 L. F. Abascal, *et al.*, *J. Chem. Phys.*, 2005, **123**, 234505.
32 J. J. Potoff and J. I. Siepmann, *AIChE J.*, 2001, **47**, 1676–1682.
33 C. L. Kong, *J. Chem. Phys.*, 1973, **59**, 2464–2467.
34 S. L. Mayo, B. D. Olafson and W. A. Goddard, *J. Phys. Chem.*, 1990, **94**, 8897–8909.
35 Y. He and N. A. Seaton, *Langmuir*, 2005, **21**, 8297–8301.
36 (*a*) D. C. Grinter, F. Venturini, P. Ferrer, M. A. van Spronsen, R. Arrigo, W. Quevedo Garzon, K. Roy, A. I. Large, S. Kumar and G. Held, *J. Synchrotron Radiat. News*, 2022, **35**(3), 39–47; (*b*) G. Held, F. Venturini, D. C. Grinter, P. Ferrer, R. Arrigo, L. Deacon, W. Quevedo Garzon, K. Roy, A. Large, C. Stephens, A. Watts, P. Larkin, M. Hand, H. Wang, L. Pratt, J. J. Mudd, T. Richardson, S. Patel, M. Hillman and S. Scott, *J. Synchrotron Radiat.*, 2020, **27**, 1153–1166.
37 P. Quinn, *et al.*, *J. Synchrotron Radiat.*, 2021, **28**, 1006–1013.
38 J. E. Parker, *et al.*, *J. Synchrotron Radiat.*, 2022, **29**, 431–438.
39 M. Lerotic, C. Jacobsen, T. Schäfer and S. Vogt, *Ultramicroscopy*, 2004, **100**, 35–57.
40 A. Gaur, D. Shrivastava and K. Joshi, *J. Phys. Conf. Ser.*, 2009, **190**, 012084.
41 M. Du, L. Li, M. Li and R. Si, *RSC Adv.*, 2016, **6**, 62705–62716.
42 G. M. Su, H. Wang, B. R. Barnett, J. R. Long, D. Prendergast and W. S. Drisdell, *Chem. Sci.*, 2021, **12**, 2156–2164.
43 P. Salén, *et al.*, *J. Chem. Phys.*, 2016, **144**, 244310.
44 R. Arrigo, *et al.*, *ACS Catal.*, 2022, **12**, 411–430.
45 Y. Chen, *et al.*, *Commun. Chem.*, 2018, **1**, 1–8.
46 H. Aitchison, H. Lu, M. Zharnikov and M. Buck, *J. Phys. Chem. C*, 2015, **119**, 14114–14125.
47 R. Arrigo, *et al.*, *ACS Catal.*, 2015, **5**, 2740–2753.
48 M. Thommes, *et al.*, *Pure Appl. Chem.*, 2015, **87**, 1051–1069.
49 E. Pérez-Botella, *et al.*, *Chem. Rev.*, 2022, **122**(24), 17647–17695.

50 A. Zárate, *et al.*, *RSC Adv.*, 2016, **6**, 9978–9983.
51 O. Shekhah, *et al.*, *Nat. Commun.*, 2014, **5**, 4228.
52 L. Grajciar, A. D. Wiersum, P. L. Llewellyn, J. S. Chang and P. Nachtigall, *J. Phys. Chem. C*, 2011, **115**, 17925–17933.
53 M. Larsson, J. B. Lindén, S. Kaur, B. Le Cerf and I. Kempson, *Powder Diffr.*, 2017, **32**, S28–S32.
54 I. Yamane, K. Sato, R. Otomo, T. Yanase, A. Miura, T. Nagahama, Y. Kamiya and T. Shimada, *Nanomaterials*, 2021, **11**, 1040.
55 V. Černý, *J. Optim. Theory Appl.*, 1985, **45**, 41–51.
56 S. Kirkpatrick, C. D. Gelatt and M. P. Vecchi, *Science*, 1983, **220**, 671–680.
57 Z. Liang, M. Marshall and A. L. Chaffee, *Energy Fuels*, 2009, **23**, 2785–2789.
58 D. Ongari, D. Tiana, S. J. Stoneburner, L. Gagliardi and B. Smit, *J. Phys. Chem. C*, 2017, **121**, 15135–15144.
59 G. M. Su, *et al.*, *Chem. Sci.*, 2021, **12**, 2156–2164.
60 N. Drenchev, *et al.*, *J. Phys. Chem. C*, 2018, **122**, 17238–17249.
61 A. Itadani, *et al.*, *Langmuir*, 2013, **29**, 9727–9733.